Hepatic angiokine IFI16/IFI202 couples endothelial senescence and stellate cell activation to drive liver fibrosis

Ga Young Lim[1,*], Seung-Su Kim[1,*], Ji-Eun Kim[1], Hae-Min Kwon[1], Na-Lee Ka[2], Hyun Young Kim[3,4], Hyeon-Ji Kim[1], Sang-Heon Lee[1], Cheolhee Jeong[1], Yun-Hee Lee[1,5], Won Kim[6], Jihye You[7], You Mie Lee[7], Soo Young Park[8], and Mi-Ock Lee[1,5,9,**]

[1]College of Pharmacy and Natural Products Research Institute, Seoul National University, Seoul 08826, Republic of Korea.

[2]College of Pharmacy, Duksung Women's University, Seoul 01369, Republic of Korea.

[3]College of Pharmacy, Dankook University, Cheonan 31116, Republic of Korea.

[4]Center for Human Risk Assessment, Dankook University, Cheonan, Chungnam, Republic of Korea

[5]Research Institute of Pharmaceutical Sciences, Seoul National University, Seoul 08826, Republic of Korea.

[6]Department of Internal Medicine, Seoul National University College of Medicine, SMG-SNU Boramae Medical Center, Seoul 07061, Republic of Korea.

[7]Research Institute of Pharmaceutical Sciences, College of Pharmacy, Kyungpook National University, Daegu 41566, Republic of Korea.

[8]Department of Internal Medicine, School of Medicine, Kyungpook National University, Daegu 41944, Republic of Korea.

[9]Bio-MAX institute, Seoul National University, Seoul 08826, Republic of Korea.

*Equal contribution

**Corresponding author. Tel: +82 2 880 9331; E-mail: molee@snu.ac.kr

Address correspondence to: Mi-Ock Lee Ph. D., College of Pharmacy, Seoul National University, 1 Gwanak-ro, Gwanak-gu, Seoul 08826, Republic of Korea. E-mail: molee@snu.ac.kr

Abstract

Liver fibrosis, a hallmark of chronic liver injury, is primarily driven by the activation of hepatic stellate cells (HSCs), while liver sinusoidal endothelial cells (LSECs) serve as upstream regulators through secretion of signaling molecules. Here, we investigated the role of interferon-γ–inducible protein 16 (IFI16) and its murine homolog IFI202 as an angiokine secreted by LSECs and a mediator of LSEC–HSC crosstalk during fibrogenesis. We observed progressive upregulation of IFI16 in both hepatic tissues and serum across advancing stages of fibrosis, as revealed by integrated analysis of bulk and single-nucleus RNA sequencing datasets together with human specimens. IFI202 expression and secretion were markedly increased in LSECs in murine models of liver fibrosis induced by CDAA-HFD, DDC diet, and CCl_4, and its release was dependent on gasdermin D–mediated mechanisms. Extracellular IFI202 enhanced HSC activation and promoted LSEC senescence both in monoculture and in multicellular liver spheroids. Genetic and pharmacologic inhibition of IFI202, via AAV-mediated knockdown or neutralizing antibodies, disrupted LSEC–HSC crosstalk and attenuated liver fibrosis. Collectively, IFI16/IFI202 represents a previously unrecognized LSEC-derived angiokine that drives hepatic fibrogenesis and may serve as both a therapeutic target and a circulating biomarker for fibrotic liver diseases.

Keywords: IFI16/IFI202, Liver fibrosis, Liver sinusoidal endothelial cells, Cellular senescence, Hepatic stellate cells, MASH

Introduction

Liver fibrosis represents a maladaptive wound-healing response to chronic hepatic injury, characterized by the excessive accumulation of extracellular matrix components [1]. It most commonly arises from metabolic dysfunction, viral hepatitis, and chronic alcohol consumption. Despite these diverse etiologies, a common pathogenic mechanism involves oxidative stress and hepatocellular injury, which stimulates liver sinusoidal endothelial cells (LSECs), Kupffer cells (KCs), and infiltrating immune cells to release inflammatory and pro-fibrotic cytokines [2]. These signals activate hepatic stellate cells (HSCs), driving their transdifferentiation into myofibroblasts, which produce excessive collagen and other extracellular matrix components, thereby disrupting liver architecture [3]. Without removal of the injurious stimulus or timely therapeutic intervention, fibrosis may progress to cirrhosis, defined by irreversible architectural distortion and impaired hepatic function. Importantly, cirrhosis is a leading cause of liver-related mortality, accounting for 2.4% of all global deaths, with liver transplantation being the only curative option [4]. Unfortunately, effective diagnostic and therapeutic strategies for liver fibrosis remain elusive due to the complex and incompletely characterized pathogenic mechanisms underlying the disease.

LSECs are highly specialized endothelial cells lining the hepatic sinusoids and represent the most abundant non-parenchymal cell population in the liver [5]. LSECs contribute to the maintenance of hepatic homeostasis through diverse functions, including regulation of vascular tone, antigen presentation, antigen clearance, intrahepatic coagulation control, and the maintenance of HSC quiescence [6]. Unlike conventional capillaries in other organs, LSECs are distinguished by the presence of fenestrae and the absence of a basement membrane, facilitating direct solute exchange between blood and hepatocytes [5]. In response to acute or chronic injury, however, LSECs undergo capillarization, a phenotypic shift characterized by the loss of fenestrae, deposition of basement membrane, acquiring a pro-fibrotic phenotype while losing their ability to maintain HSC quiescence [7]. Furthermore, capillarized LSECs secrete pro-fibrotic mediators, including adipocyte fatty acid–binding protein, endothelin-1, EIIIA-fibronectin, and extracellular vesicles carrying sphingosine kinase 1, to sustain HSC activation [8]. Thus, beyond the traditional HSC-centric paradigm, LSECs are

increasingly recognized as active regulators of fibrosis. However, the molecular mechanisms underlying these changes and the regulation of their angiocrine function during liver fibrogenesis are insufficiently understood.

Interferon-γ-inducible protein 16 (IFI16) is an intracellular pattern recognition receptor that detects aberrant or foreign double-stranded DNA, playing a key role in innate immunity [9]. Chronic DNA damage and oxidative stress induce upregulation of IFI16, which promotes cellular senescence in multiple cell types including endothelial cells [10]. The IFI16–cyclic GMP–AMP synthase (cGAS)–stimulator of interferon genes (STING) signaling cascade activates interferon regulatory factor 3 and NF-κB, inducing type I interferon (IFN) and inflammatory cytokines in keratinocytes and monocytes [11]. We previously showed that IFI16 impairs DNA repair, resulting in cytosolic DNA accumulation which activates the cGAS–STING signaling [12]. Recently, an important role of the cGAS–STING signaling has been recognized in the liver, particularly in pathological conditions. Release of mitochondrial DNA from injured hepatocytes or HSCs activates the cGAS–STING pathway triggering inflammatory and pro-fibrotic responses during progression of metabolic dysfunction–associated steatotic hepatitis (MASH) [13, 14]. Multi-omics analyses showed that elevated hepatic expression of specific IFI16 variants were associated with the progression of metabolic dysfunction–associated steatotic liver diseases (MASLD) [15]. Although these observations suggest that IFI16-associated inflammatory signaling evokes pro-fibrotic responses during the progression of liver fibrosis, the cellular and molecular mechanisms are still poorly understood.

Our previous work demonstrated that IFI202, a murine homolog of IFI16, was secreted by breast cancer cells into circulation in mice, where the IFI200 family member stimulated macrophage cytokine production, creating immunosuppressive tumor microenvironment [16]. Extracellular IFI16 has also been detected in the sera of patients with autoimmune diseases, including Sjögren's syndrome, rheumatoid arthritis, and systemic lupus erythematosus [17-19]. Upon ultraviolet stimulation, IFI16 was released into the extracellular space, functioning as a damage-associated molecular pattern (DAMP) that induced expression of inflammatory cytokines and chemokines via the TLR4 pathway [20]. Together, these observations raise the possibility that IFI16 may exert extracellular functions in the

fibrotic liver, prompting us to investigate its pathogenic role in sinusoidal signaling and fibrogenesis.

Materials and methods

Analysis of public bulk and single-cell transcriptomic datasets

Public human liver RNA-seq datasets were obtained from the NCBI Gene Expression Omnibus under accession numbers GSE256398, GSE206364, GSE244832, GSE151158, GSE193066, GSE159676, and GSE79850. Raw count matrices were directly imported into R (v4.4.3) and analyzed using DESeq2 (v1.46.0). Differential gene expression analysis was performed between healthy and MASH groups with significance thresholds set at $\log_2$fold-change > 0.5 and adjusted p-value < 0.0001. IFI16 expression levels were specifically interrogated across different disease stages. Single-nucleus RNA sequencing (snRNA-seq) data from GSE244832 were analyzed using Seurat (v5.3.0) in R with a pipeline optimized for snRNA-seq data as described previously [21]. Data were log-normalized, and highly variable features were identified. To correct for inter-sample batch effects, Harmony integration [22] was applied prior to clustering. Low-quality and sample-specific clusters were removed according to the quality control criteria described in the original study, followed by re-clustering using the Leiden algorithm. Cell type annotation was performed using marker gene sets from PanglaoDB [23] combined with hypergeometric enrichment analysis, enabling systematic and liver-specific classification. Dimensional reduction and visualization were conducted using UMAP with a cosine distance metric. IFI16 expression was examined across cell clusters and disease conditions. Plots were generated using ggplot2 (v3.5.2) and patchwork (v1.3.0). Gene Set Variation Analysis using Hallmark gene sets was performed to assess pathway activity, followed by correlation analysis with IFI16 expression.

Human samples

Liver tissue samples from normal, MASL and MASH patients were obtained from the Seoul Metropolitan Government Boramae Medical Center (Seoul, Korea) under institutional review board approval (IRB No. 16-2014-86) [21]. Human serum samples from normal, and patients with MASL and cirrhosis were obtained from the Department of Internal Medicine, School of Medicine, Kyungpook National University (Daegu, Korea) under institutional review board approval (IRB No. KNUH 2014-

04-056-015), as previously described [24].

Animal experiments

All animal procedures were approved by the Institutional Animal Care and Use Committee of Seoul National University (SNU-230602-2-1 and SNU-221214-1-1). Liver fibrosis was induced by feeding mice either a choline-deficient, L-amino acid-defined, high-fat diet (CDAA-HFD, Research Diets Inc) for 7 weeks, or a diet containing 0.1% 3,5-diethoxycarbonyl-1,4-dihydrocollidine (DDC, Sigma-Aldrich) for 2 weeks followed by normal chow for a week. The DDC diet was prepared by thoroughly mixing 0.1% (w/w) DDC into a standard chow diet. Also liver fibrosis was induced by intraperitoneal injection of CCl_4 (Sigma-Aldrich; diluted in corn oil, 50 μL/100 g body weight) twice weekly for 4 weeks.

To investigate the role of IFI202, an AAV vector encoding shRNA against IFI202, designated as AAV9-sh*Ifi202* (AAV9-U6-IFI202-sh-CMV-EGFP), and a scrambled control virus, designated as AAV9-shControl (AAV9-U6-SCR-CMV-EGFP), were constructed using standard DNA recombination technique with a pAAV-MCS backbone vector (Cell Biolabs) under the control of a CMV promoter and were packaged using an AAV9 serotype. AAV particles were produced in HEK293T cells at the Virus Facility of the Korea Institute of Science and Technology (Seoul, Korea). The AAV (1×10^{11} genome copies in 100 μL) was delivered to mice by a retro-orbital injection.

Recombinant IFI202 protein tagged with a C-terminal His-tag was produced as previously described [16]. rIFI202 was diluted in PBS, sterilized by filtration, and intraperitoneally injected daily for 2 weeks. At the end of experiments, mice were anesthetized and blood was collected via cardiac puncture. Serum levels of AST, ALT, BUN, and total bilirubin were measured using a FUJI DRI-CHEM 3500s analyzer. Liver lobes were excised and fixed in 10% neutral buffered formalin for paraffin embedding or embedded in optimal cutting temperature compound for cryosection preparation.

Total nitrate/nitrite levels in mouse plasma and conditioned media collected from primary LSECs were measured using a nitric oxide assay kit (Abcam) according to the manufacturer's instructions. Absorbance was measured at 540 nm, and total nitrate/nitrite concentrations were

calculated from the standard curve.

Isolation of mouse liver cells and culture

Primary mouse hepatocytes were isolated from 8–10-week-old male C57BL/6N mice as described previously [25]. HSCs, LSECs, and KCs were obtained from the non-parenchymal fraction by centrifugation in a discontinuous Percoll gradient. The top layer enriched in HSCs was collected. LSECs were isolated from the intermediate layer by magnetic-activated cell sorting using CD146 microbeads (Miltenyi Biotech). The unbound fraction remaining after magnetic-activated cell sorting separation was collected as KCs. Isolated cells were suspended in DMEM supplemented with 10% fetal bovine serum. Experiments with primary LSECs were completed within 24 h to preserve their endothelial phenotype. TLR2 signaling in HSCs was inhibited by treatment with C29 (InvivoGen) or OxPAPC (InvivoGen), or by TLR2 siRNA transfection using Lipofectamine 3000 (Invitrogen) according to the manufacturer's instructions.

To determine senescence-associated β-galactosidase (SA-β-gal) activity, primary LSECs were stained using the senescence cells histochemical staining kit (Sigma-Aldrich) according to the manufacturer's instructions. Briefly, cells were fixed for 6 min, incubated with the staining mixture at 37°C without CO_2, and imaged by light microscopy. SA-β-gal-positive cells were identified by blue staining and quantified as a percentage of the total cells. Lactate dehydrogenase (LDH) release assays were performed using an LDH cytotoxicity assay kit (Sigma-Aldrich) according to the manufacturer's instructions. The LDH activity in culture media were normalized to Tergitol-induced total lysis, which served as the positive control and was defined as 100% maximal LDH release.

Mouse liver spheroids were generated by combining hepatocytes, non-parenchymal cells including myeloid cells, endothelial cells, T cells, B cells, and NKT cells, and HSCs at proportions adjusted to approximate the physiological cellular composition of human MASH livers [26]. Specifically, hepatocytes, non-parenchymal cells, and HSCs were seeded into 96-well plates and cultured on an orbital shaker. Culture medium was replaced with fetal bovine serum-free fresh medium every 2 days. On day 3 of post-seeding, spheroids were treated with rIFI202 for 7 days. At the end of

treatment, spheroids were harvested for immunofluorescence staining and western blot analysis.

Western blotting, Immunoprecipitation, ELISA, immunohistochemistry and qRT-PCR

Western blotting and immunoprecipitation were performed as previously described using specific antibodies (Supplementary Table 1) [16]. For analysis of secreted proteins, serum-free culture supernatants were precipitated with 20% trichloroacetic acid, washed with cold acetone, and subjected to western blotting. Concentrations of IFI16, IFI202, IL-1β, IL-6, and TNF-α in serum or culture supernatants were measured using ELISA kits. For immunofluorescence, specimens were fixed in ice-cold methanol or 4% paraformaldehyde and stained as previously described [12]. Fluorescent images were acquired and analyzed using a confocal microscope and LAS X software. For immunohistochemistry, sections of paraffin-embedded tissue were stained with specific antibodies and examined using an automated multimodal tissue analysis system. The mRNA levels were determined by qRT-PCR using an ABI StepOnePlus™ Real-time PCR system with specific primers (Supplementary Table 2). Relative mRNA expression was calculated relative to controls using the $2^{-\Delta\Delta CT}$ method [27].

Neutralizing anti-IFI202 antibodies

rIFI202 was used for mouse immunization and monoclonal antibody generation. Hybridomas were generated by electrofusion of spleen cells with SP2/0 myeloma cells, selected in HAT medium, and screened by ELISA for binding to rIFI202. Functional screening involved assessing suppression of IL-6 production in bone marrow–derived macrophages stimulated with 4T1-conditioned medium. Clones with the highest inhibitory activity were subcloned. The isotypes of monoclonal antibodies were determined using the Isostrip Mouse Monoclonal Isotyping kit (Roche) and SBA Clonotyping System-HRP kit (SouthernBiotech). Antibodies were purified from hybridoma supernatants using protein A–coated magnetic beads (GenScript). Purified antibodies were dialyzed against phosphate-buffered saline (pH 7.2–7.4) and stored at 2–8 °C until use. The production of the neutralizing antibody was performed by Hana Pharmaceutical Co., Ltd (Seoul, Korea). For animal experiments, either control IgG or

neutralizing anti-IFI202 antibody at a dose of 150 μg in 150 μL PBS was intraperitoneally injected to mice every other day for a total of three weeks.

Statistical analysis

The number of samples is indicated in the figure legends, and three or four independent biological experimental replicates were conducted. All analyses were performed using GraphPad Prism software. Statistical analyses between two groups were conducted using the nonparametric Mann–Whitney *U* test (two-tailed). For experiments with $n = 3$ biological replicates, statistical significance was determined using an unpaired *t*-test, assuming a normal (Gaussian) distribution. When the experiments contain more than two groups, differences between groups were analyzed using one-way ANOVA. Statistical analyses of multiple groups were performed using two-way ANOVA followed by the Bonferroni posttest. Data are presented as the mean ± SD or the mean ± SEM, as indicated in figure legends. Statistical significance was set at $P < 0.05$.

Supplementary Table 1 provides detailed information on the materials.

Results

Hepatic and circulating IFI16 levels are elevated in patients with progressive liver fibrosis

To better understand the underlying pathophysiology associated with the development of liver fibrosis at the molecular level, we performed a differential gene expression analysis using publicly available RNA sequencing datasets of liver tissues from patients with progressive MASH (GSE256398, GSE206364, and GSE244832). By applying thresholds of $\log_2$ fold-change > 0.5 and $p < 0.0001$, we identified 21 genes consistently upregulated across all three datasets (Figure 1A, Supplementary Table 3). Among these genes, we were interested in IFI16, since it has been predominantly recognized as an intracellular DNA sensor that amplifies cGAS–STING and NF-κB signaling, eventually leading to sustained inflammatory signaling and cellular senescence [11]. Further analysis of chronic liver disease datasets showed a progressive upregulation of IFI16 expression along with advanced disease stages of MASLD. Moreover, elevated levels of hepatic IFI16 transcripts were also observed in patients with cholestatic liver diseases, including primary biliary cholangitis, primary sclerosing cholangitis, and autoimmune hepatitis, suggesting that IFI16 upregulation is a common feature across diverse etiologies of chronic liver injury, potentially with fibrotic changes (Figure 1B).

To delineate the cellular sources of IFI16 within the liver, we analyzed single-nucleus RNA sequencing data from 18 individuals with varying MASLD stages (GSE244832), encompassing nine liver cell types. Across all cell types, IFI16-positive cells were most abundant in LSECs, accounting for approximately 50% of IFI16-expressing cells. Notably, IFI16 expression was predominantly enriched in LSEC and showed a marked increase in MASH, identifying LSECs as the principal cellular source of IFI16 in diseased liver (Figure 1C). To further characterize IFI16-associated transcriptional programs, we performed gene set variation analysis-based correlation assessment. In LSECs, IFI16 expression was associated with inflammatory and endothelial activation pathways, including IFN-γ response, IL2/STAT5 signaling, and apical junction, all of which progressively increased with disease severity (Supplementary Figure 1A). These findings indicate that IFI16 expression in LSECs is closely associated with endothelial dysfunction during MASH progression.

We next examined whether IFI16 was associated with pathogenic programs in other nonparenchymal cell populations. In HSCs, IFI16-correlated transcriptional programs were enriched for fibrogenic and tissue-remodeling pathways, including TGF-β signaling and angiogenesis. In Kupffer cells, IFI16 expression was associated with inflammatory and immune-related pathways, including IL-6/JAK/STAT3, IL-2/STAT5, IFN-γ response, and TGF-β signaling, several of which also became progressively enriched during disease progression. These analyses suggest that, although IFI16 is most prominently enriched in LSECs, its expression is also associated with distinct pathogenic transcriptional programs in multiple hepatic nonparenchymal cell populations during MASH progression (Supplementary Figure 1A).

We performed immunohistochemistry to assess IFI16 expression in liver tissues from patients with metabolic dysfunction–associated steatotic liver (MASL) and MASH. As shown in Figure 1D, IFI16 protein levels in liver increased progressively with MASLD severity. Since elevated circulating IFI16 level has been reported in patients with certain autoimmune diseases such as systemic lupus erythematosus [19], we assessed circulating levels of IFI16 in the serum obtained from normal individuals, patients with MASL and those with cirrhosis [24]. Strikingly, serum IFI16 levels increased in a stage-dependent manner, with the highest concentrations detected in patients with cirrhosis (Figure 1E). Receiver operating characteristic curve analysis suggested that circulating IFI16 has diagnostic potential for distinguishing healthy controls from patients with liver disease and patients with MASL from those with cirrhosis; however, these findings should be interpreted with caution given the limited cohort sizes and require validation in larger and independent cohorts (Supplementary Figure 1C).

IFI202 levels in the liver and the serum are increased after fibrosis-inducing liver injury in mice

To investigate the role of IFI202, a mouse homolog of IFI16, in the progression of chronic liver diseases, we employed diverse mouse models of liver injury [28]. First, mice were fed CDAA-HFD to develop MASH (Figure 2A). Similar to the observation in patients with MASH, IFI202 was markedly upregulated in the liver of MASH mice (Figure 2A). Western blot further confirmed elevated IFI202 expression in the liver of CDAA-HFD-fed mice whereas expression of other IFI200 family members,

such as IFI203 and IFI204, was not altered. Increases in the levels of pSTING/STING and IFN-β, which are downstream effectors of IFI16/IFI202 signaling, were observed in the mouse livers (Figure 2A, Supplementary Figure 2). Similarly, hepatic IFI202 protein levels were markedly elevated in mice fed DDC diet, as well as in mice treated with CCl_4, a hepatotoxicant that induces oxidative stress and promotes fibrosis (Figures 2B, 2C and Supplementary Figure 2). Interestingly, serum IFI202 levels were markedly increased in these mouse models of fibrosis-inducing liver injury (Figure 2D). Transcripts of *Ifi202* were largely increased in livers of these mice, suggesting a transcriptional regulation of *Ifi202* under the fibrotic liver microenvironment (Figure 2E).

IFI202 is secreted from the LSECs under cellular stress *via* pore-forming protein gasdermin D

Immunofluorescence staining of liver tissues from DDC diet–fed mice also demonstrated increased expression of IFI202. Notably, IFI202 co-localized with CD31, a marker of capillarized LSECs in DDC diet- and CDAA-HFD-fed mice (Figure 3A and Supplementary Figure 3A). Moreover, co-staining with LYVE1, which is enriched in LSECs at zones 1–2, and KIT, present in a peri-central region, revealed that IFI202 was primarily localized to endothelial cells in the peri-portal region (Figure 3B) [29]. Interestingly, IFI202 expression was broadly increased in LSECs across zones 1–3 in CDAA-HFD-fed mice, indicating that the spatial distribution of injury-induced IFI202 appears to vary according to the underlying etiology (Supplementary Figure 3B). To support this observation, IFI202 expression was analyzed in the isolated hepatocytes and non-parenchymal cells from mouse liver. IFI202 was mainly expressed in the LSECs of normal mice and much higher in the LSECs obtained from CCl_4-treated mice (Figure 3C). Treatment with IFN-β increased both the expression and secretion of IFI202 in the LSECs under culture conditions that preserved their endothelial phenotype. IFN-β treatment did not increase LDH release in the same conditions, indicating that IFI202 release is not attributable to secondary leakage caused by cytotoxicity (Figure 3D). In addition, treatment with hydrogen peroxide, pro-fibrogenic cytokines such as IL-6 and TGF-β, and chenodeoxycholic acid led to induction and secretion of IFI202 from the LSECs (Figure 3E, Supplementary Figure 3C). Given that activated KCs and HSCs serve as a major source of IL-6 and TGF-β during fibrogenesis, these findings suggest a potential

paracrine signaling could promote IFI202 release from LSECs in the fibrotic liver [30].

Many proteins lacking classical signal peptides, such as high mobility group box 1, have also been reported to be released via gasdermin D (GSDMD) pores [31]. Since IFI202 lacks a signal peptide, we suspected that it may also utilize GSDMD for its secretion. To explore a possible association between IFI202 and GSDMD, we performed co-immunoprecipitation assays, which revealed an association between the two proteins (Figure 4A). An *in vitro* co-immunoprecipitation assay using purified recombinant proteins, further demonstrated that IFI202 physically binds to GSDMD (Figure 4B). When LSECs were treated with necrosulfonamide, an inhibitor of GSDMD, the levels of secreted IFI202 in the culture media were significantly reduced, demonstrating that IFI202 secretion depends on GSDMD-mediated pore formation (Figure 4C). Lastly, treatment of LSECs with hydrogen peroxide increased expression of not only IFI202 but also GSDMD when measured by western blot and immunofluorescence (Figure 4A, 4D). Co-localization of these proteins was evident in the LSECs when cells were treated with hydrogen peroxide (Figure 4D).

Knockdown of IFI202 alleviates DDC diet-induced fibrosis

As IFI202 was predominantly expressed in liver endothelial cells (Figure 3C), we adopted a liver-targeted knockdown approach using AAV9, which efficiently transduces hepatic tissues. To establish a causal role for IFI202 in liver fibrosis, the DDC diet model was selected as it has been widely used in studies investigating LSEC dysfunction and liver microvascular remodeling during fibrosis [32]. Mice fed a DDC diet were administered either AAV9-sh*Ifi202*, encoding an shRNA targeting *Ifi202*, or a scrambled control virus (AAV9-shControl). Infusion of the AAV9-sh*Ifi202* partially recovered body weight that was decreased upon DDC diet feeding. AST and ALT levels markedly reduced by the AAV9-mediated *Ifi202* knockdown (Figure 5A). Histological analysis showed a decreased Sirius Red–positive area in the livers of AAV9-sh*Ifi202* infused mice relative to control livers. The hepatic expression levels of collagen type I alpha 2 (COL1A2) and α-smooth muscle actin (αSMA) were markedly reduced in the AAV9-sh*Ifi202* infused mice, indicating that the function of IFI202 is associated with liver injury and hepatic fibrogenesis (Figure 5B, Supplementary Figure 4). Since

activation of GSDMD has been implicated in cellular senescence, we examined the involvement of IFI202 in cellular senescence [33]. SA-β-galactosidase staining showed that the number of senescent cells was significantly reduced in the AAV9-sh*Ifi202* infused group. Levels of pSTING and p21 were notably decreased, suggesting that IFI202 was involved in the senescence-associated pathways (Figure 5C, Supplementary Figure 4). Expression of LYVE1 was restored after knockdown of IFI202 (Figure 5D). Consistently, mRNA levels of multiple LSEC functional genes, such as *Cd209b* and *Lyve-1*, were restored after knockdown of *Ifi202*, indicating a negative role of IFI202 in the function of LSECs (Figure 5D).

Recombinant IFI202 induces fibrotic changes in the mouse liver

To validate the fibrogenic potential of IFI202 in the liver, recombinant IFI202 protein (rIFI202) was intraperitoneally injected into mice. Body weight decreased, whereas serum AST and ALT levels increased, indicating hepatic injury in the rIFI202-treated mice (Figure 6A). ELISA assay further revealed dose-dependent increases in circulating inflammatory cytokines, including IL-6, TNF-α, and IL-1β (Figure 6B). Levels of COL1A2, αSMA, TGF-β, and pSMAD3 were elevated dose-dependently (Figure 6C, Supplementary Figure 5), Consistently, collagen deposition and αSMA expression level were elevated in the livers of rIFI202-treated mice (Supplementary Figure 5). In addition, SA-β-gal staining revealed increased senescence in the livers of rIFI202-injected mice, accompanied by elevated levels of pSTING, p21, and N-GSDMD, which may underline the mechanism of cellular senescence and extracellular release of IFI202 (Figure 6D, Supplementary Figure 5). To assess the human relevance of these findings, treatment with recombinant IFI16 proteins upregulated expression of COL1A1 and αSMA in LX-2 human HSCs (Supplementary Figure 6). Together, these results indicate that rIFI202 protein alone is sufficient to induce hepatic fibrogenesis, inflammation, and senescence-associated changes in the liver.

Next, we examined the effects of rIFI202 on the primary HSCs and LSECs to understand the mechanism by which IFI202 contributes to liver fibrosis at the cellular level. Considering that IFI202 has been shown to signal through TLR2 and that both HSCs and LSECs express functional TLR2, we

speculated that rIFI202 activates downstream signaling *via* this pathway [16, 34]. We observed that the addition of rIFI202 accelerated the activation of primary HSCs in culture, accompanied by increased αSMA expression and activation of canonical fibrogenic signaling pathways (Figure 7A, Supplementary Figure 7A). Interaction between IFI16 and TLR2 was demonstrated by co-immunoprecipitation in LX-2 cells overexpressing tagged IFI16 and TLR2 (Supplementary Figure 7B). rIFI202 treatment markedly increased the phosphorylation of ERK and p65, key downstream effectors of TLR2 signaling (Figure 7B, Supplementary Figure 7C). Notably, pharmacological inhibition of TLR2 using C29 or OxPAPC, or siRNA-mediated knockdown of TLR2 significantly attenuated rIFI202-induced phosphorylation of both ERK and p65, indicating that IFI202-mediated HSC activation occurs via a TLR2-dependent mechanism (Figure 7C, Supplementary Figure 7D, 7E) [35].

Treatment of primary LSECs with rIFI202 decreased the expression levels of the differentiation markers of LSECs, such as *Cd209b* and *Lyve1*, supported a phenotypic shift away from healthy sinusoidal function (Figure 7D). Consistent with our in *vivo* findings, treatment of primary LSECs with rIFI202 induced multiple features of cellular senescence, including reduced nuclear LAMIN B1 expression, a marker of nuclear integrity, and increased p21 expression (Figure 7E). Furthermore, rIFI202 significantly increased SA-β-gal activity compared with vehicle-treated controls. Importantly, the rIFI202-induced senescence phenotype was markedly attenuated by treatment with C-176, a selective covalent inhibitor of murine STING that blocks STING activation and its downstream signaling (Figure 7F). Collectively, these findings demonstrate that extracellular IFI202 is sufficient to induce senescence-associated changes in primary LSECs and that this process is functionally dependent on STING activation.

To support these findings in a more physiologically relevant context, we established a three-dimensional mouse liver spheroid model [36]. Treatment with rIFI202 resulted in increased expression of αSMA, COL1A2, TGF-β, and p21 within the liver spheroids (Figure 7G). Collectively, these data indicate that IFI16/IFI202 mediates both paracrine and autocrine signaling in the fibrotic liver, activating HSCs and inducing LSEC senescence. In conjunction with the findings in Figure 3E, these results collectively delineate a feed-forward regulatory circuit in which IFI202 acts as a key mediator

of intercellular crosstalk during liver fibrogenesis.

Neutralizing IFI202 alleviates DDC diet-induced fibrosis

To further validate the role of IFI202 as a key mediator of fibrogenic crosstalk, we generated a neutralizing antibody specific to IFI202 and examined the effects of its blockade. Since cultured LSECs progressively acquire a stress-activated phenotype characterized by activation of inflammatory pathways together with increased expression and secretion of inflammatory mediators, primary HSCs were cultured in the conditioned medium (CM) obtained from LSECs that were pre-treated with either the anti-IFI202 Ab or control IgG [37]. Activation of HSCs was attenuated by culturing with the CM pretreated with anti-IFI202 Ab, indicating that soluble IFI202 in the CM plays a direct role in promoting HSC activation (Figure 8A). Moreover, administration of anti-IFI202 Ab in the DDC diet-fed mice significantly attenuated liver injury, as shown by restored body weight and reduced serum AST, ALT, BUN and total bilirubin levels (Figure 8B). Histological and immunofluorescence analyses showed a marked decrease in collagen deposition and αSMA expression. Additionally, the levels of LYVE1 as well as multiple LSEC differentiation markers were restored, whereas mRNA levels of capillarized LSEC markers, *Pecam1* and *Edn1*, were reduced, suggesting improved maintenance of LSEC identity. Consistently, the expression of fibrotic and senescence markers was also attenuated (Figure 8C, 8D, and Supplementary Figure 8A). Similarly, administration of anti-IFI202 Ab in the CCl_4-treated mice attenuated liver injury and fibrosis as shown in Figure 8E-8G, Supplementary Figure 8B. Anti-IFI202 Ab administration did not induce detectable toxicity in major extrahepatic organs under the experimental conditions. Also, it did not significantly alter the proportion of neutrophils or any other major immune cell populations compared with the IgG control (Supplementary Figure 8C, 8D). Together, these results support a broader pathogenic role of IFI202 across distinct etiologies of liver fibrosis and suggest potential therapeutic strategies against these diseases.

To further determine whether IFI202 inhibition functionally restores endothelial function, we assessed eNOS signaling and nitric oxide production. In line with the restored expression of LSEC functional markers, anti-IFI202 Ab-treated liver tissues exhibited increased phosphorylation of eNOS,

total eNOS expression, and plasma nitric oxide levels were elevated in both DDC diet-fed and CCl_4-treated mice (Figure 8H, 8I, Supplementary Figure 8E). We further validated these findings in primary LSECs. First, rIFI202 treatment increased the phosphorylation of STING and IRF3, which was attenuated by anti-IFI202 Ab treatment in primary LSECs, confirming the involvement of STING–IRF3 axis in the IFI202-mediated signaling in LSECs. rIFI202 treatment significantly suppressed p-eNOS expression, indicating impaired eNOS activation, and reduced nitric oxide levels in the conditioned medium. Importantly, these effects were fully reversed by neutralization with anti-IFI202 Ab (Figure 8J). Collectively, these results establish that IFI202 impairs endothelial function and that its inhibition effectively restores eNOS activity and nitric oxide production.

Discussion

LSECs are increasingly recognized as central regulators of fibrogenic microenvironments during progression of liver fibrosis. For example, in pathogenesis of MASH, LSECs secreted angiocrine factors, including CXCL chemokines and angiopoietin-2, which promote leukocyte recruitment, endothelial inflammation, and pathological angiogenesis in early disease. As the disease advances, LSECs acquire a pro-fibrogenic phenotype, releasing angiokines such as adipocyte fatty acid–binding protein that activates HSCs and facilitates extracellular matrix deposition [8, 38, 39]. In this study, we identify IFI16/IFI202 as a novel angiocrine factor that integrates inflammatory and fibrogenic signaling across KCs, LSECs, and HSCs through autocrine and paracrine mechanisms, thereby coordinating microenvironmental remodeling during progression of liver fibrosis.

IFI16/IFI202 has been well recognized as a cytosolic DNA sensor responding to diverse cellular stresses, including oxidative stress and viral or bacterial infection [9, 10]. Upon binding cytosolic DNA, it activates the cGAS–STING pathway, leading to production of inflammatory mediators, such as type I IFN, IL-6, and the chemokine C–C motif chemokine ligand 20 [11]. Here, we extend this understanding by revealing a DAMP-like function of IFI202. While previous work has suggested extracellular roles for IFI16/IFI202, the mechanistic link between its cytosolic DNA sensing activity and potential as a DAMP remain unclear [16, 19, 20]. Our data suggests that severe metabolic and inflammatory stress induces IFI202 expression, likely through DNA damage and accumulation of cytosolic DNA. Cytosolic DNA in turn triggers inflammasome assembly and caspase-1 activation, leading to cleavage of GSDMD, whose N-terminal fragment forms plasma membrane pores [40]. Consistent with this mechanism, extracellular release of IFI202 was suppressed by the GSDMD inhibitor NSA, implicating that IFI202 secretion occurs via GSDMD-dependent membrane pores (Figure 4). Functionally, LSEC-derived IFI16/IFI202 promoted production of IL-6, TNF-α and IL-1β from KCs, demonstrating its role as a DAMP (Supplementary Figure 9). These findings support a dual function for IFI16/IFI202: intracellularly as a cytosolic DNA sensor of cellular damage and extracellularly as a DAMP that amplifies inflammatory signaling in the hepatic microenvironment. Further studies across different cell types will be critical to determine whether these dual functions are

broadly applicable, which would strengthen the rationale for targeting IFI16/IFI202 in inflammation-associated diseases.

Our findings also suggest that IFI16/IFI202 may represent a link between hepatic injury and systemic complications in MASLD. We observed that circulating IFI16/IFI202 was markedly elevated in both MASH patients and murine models, and that administration of rIFI202 induced systemic inflammation with increased IL-1β, IL-6, and TNF-α (Figure 1E, Figure 2D and Figure 6B). These results imply that IFI16/IFI202 functions not only as a marker of hepatic injury but also as an active mediator of extrahepatic pathobiology. This concept is consistent with prior observations that an angiocrine mediator derived from dysfunctional LSECs, leucine-rich alpha-2-glycoprotein 1, was elevated in the serum of patients with MASLD, which contributed to pathological conditions of renal fibrosis and arthritis [24, 41, 42]. Mechanistically, murine IFI202 interacts with TLR2, while human IFI16 binds TLR4, a pathway implicated in renal fibrosis, nephropathy, and muscle atrophy [16, 20, 43]. These findings raise the possibility that IFI16/IFI202–TLR signaling constitutes a shared axis underlying the multi-organ involvement of MASLD. Clinically, elevated serum IFI16 has been reported in patients with systemic lupus erythematosus, many of whom also display abnormal liver function [19, 44]. Given that TLR4 is broadly expressed across hepatic cell types and actively involved in injury responses, increased circulating IFI16 levels from diverse pathological conditions could further amplify hepatic inflammation and fibrosis. Together, these data point to IFI16/IFI202 as a potential driver of liver–multiorgan crosstalk. However, a limitation of this study is the absence of an LSEC-specific conditional knockout model for IFI202. Although our AAV-mediated knockdown supports the functional role of IFI202 in liver fibrosis, this approach does not allow us to specifically define the LSEC-specific contribution of IFI202. Future studies using LSEC-specific conditional knockout mice or AAV systems driven by endothelial-specific promoters will be necessary to more precisely define the role of LSEC-derived IFI202 in liver fibrosis.

Notably, the spatial and transcriptional patterns of IFI16/IFI202 suggest a context-dependent function in LSECs. In the normal liver, IFI16 was broadly distributed in CD31-positive LSECs along the porto-central axis, and IFI16-high LSECs exhibited transcriptional programs associated with DNA

repair, p53 signaling, oxidative phosphorylation, and cellular stress responses (Supplementary Figure 1B). These findings suggest that basal IFI16 may contribute to genome surveillance and adaptive stress responses that maintain LSEC homeostasis. During chronic liver injury, however, IFI16/IFI202 was markedly induced in an etiology-dependent spatial pattern. IFI202 was preferentially increased in periportal LSECs following DDC-induced cholestatic injury, whereas CDAA-HFD induced a broader increase across zones 1–3, suggesting that its spatial induction reflects the regional pattern of LSEC stress rather than an intrinsically periportal-specific function (Figure 3B, Supplementary Figure 3B). Importantly, our functional studies showed that sustained IFI202 elevation promotes LSEC senescence and dysfunction and, following extracellular release, activates HSCs to facilitate fibrogenesis (Figure 7). Together, these findings suggest a transition from a potentially homeostatic role of basal IFI16 in LSECs to a pathological stress response during chronic injury that promotes endothelial dysfunction and fibrogenic remodeling.

The rising prevalence of obesity and metabolic syndrome has markedly increased the global burden of cirrhosis, which progresses stepwise from MASL to MASH [45]. Currently, resmetirom and semaglutide are the FDA-approved therapeutic drugs for MASH with moderate-to-advanced liver fibrosis, primarily targeting metabolic abnormalities [46]. Other investigational agents, such as efruxifermin, an FGF21 analog, are under clinical trials, exerting mainly metabolism-mediated effects with secondary benefits on fibrosis (NCT05039450). However, once HSCs enter the perpetuation phase and acquire a stabilized pro-fibrotic phenotype, the therapeutic efficacy of metabolism-targeting interventions diminishes substantially, underscoring the need for therapies that directly target fibrosis. In this regard, inhibition of TGF-β has received much attention with diverse strategies including neutralizing antibodies [47]. Nonetheless, systemic blockade of TGF-β poses significant safety concerns, given its pleiotropic roles in immune tolerance, tissue homeostasis, and tumor suppression [48]. In this context, we propose IFI16/IFI202 as a novel therapeutic target during the amplified fibrotic response. Notably, IFI16/IFI202 displays an injury-inducible secretion profile, which may reduce the risk of systemic side effects compared with broadly acting cytokine pathways. Furthermore, blockade of IFI16/IFI202 has the potential to interrupt multiple fibrogenic cascades originated from LSECs, KCs,

and HSCs. Thus, blockade of IFI16/IFI202 represents a fibrosis-focused strategy that is mechanistically distinct from metabolic modulation. Therapeutic strategies directed at IFI16/IFI202 could therefore be combined with metabolism-regulating agents, thereby expanding the treatment landscape for patients with advanced MASH.

In summary, we identify IFI16/IFI202 as secreted angiokines from liver sinusoidal endothelial cells that contribute to liver fibrosis by promoting endothelial senescence and hepatic stellate cell activation. IFI202 secretion is mediated by gasdermin D, and its inhibition through genetic or antibody-based strategies attenuates fibrosis and restores endothelial function. These findings support IFI16/IFI202 as potential biomarkers and therapeutic targets in chronic liver disease.

List of Abbreviations

AAV, adeno-associated virus; CDAA-HFD, choline-deficient, L-amino acid-defined, high-fat diet; cGAS, cyclic GMP–AMP synthase; CM, conditioned medium; COL1A2, collagen type I alpha 2; DAMP, damage-associated molecular pattern; DDC, 3,5-diethoxycarbonyl-1,4-dihydrocollidine; GSDMD, gasdermin D; HSCs, hepatic stellate cells; IFI16, Interferon-γ-inducible protein 16; IFN, interferon; KCs, Kupffer cells; LSECs, liver sinusoidal endothelial cells; MASH, metabolic dysfunction–associated steatotic hepatitis; MASL, metabolic dysfunction–associated steatotic liver; MASLD, metabolic dysfunction–associated steatotic liver disease; rIFI202, Recombinant IFI202 protein; STING, stimulator of interferon genes; αSMA, α-smooth muscle actin.

Ethical Approval and Consent to participate

The research protocol was reviewed and approved by the institutional review board of the Seoul Metropolitan Government Boramae Medical Center (IRB No. 16-2014-86) and Kyungpook National University Hospital (IRB No. KNUH 2014-04-056-015). The study was performed in accordance with the Declaration of Helsinki. All animal procedures were approved by the Institutional Animal Care and Use Committee of Seoul National University (SNU-230602-2-1 and SNU-221214-1-1) and were performed in accordance with its guidelines.

Consent for publication

Not applicable.

Availability of supporting data

Not applicable.

Conflicts of interest

The authors declare no potential conflicts of interest.

Authors' contributions

Ga Young Lim, Seung-Su Kim and Mi-Ock Lee designed the study and interpreted the results; Ga Young Lim, Seung-Su Kim, Ji-Eun Kim, Hae-Min Kwon, Na-Lee Ka, Hyeon Young Kim, Hyeon-Ji Kim, Sang-Heon Lee, Cheolhee Jeong, and Yun-Hee Lee performed the experiments and interpreted data; Won Kim, Jihye You, You Mie Lee and Soo Young Park contributed to analyzing human specimens; Ga Young Lim and Mi-Ock Lee wrote the manuscript; Mi-Ock Lee supervised the research. All authors read and approved the final manuscript.

Acknowledgements

This project was supported by the Research Grant from Seoul National University, the National Research Foundation of Korea (RS-2026-25517589 and RS-2026-25474307), and the Ministry of Education (MOE)/the Seoul Metropolitan Government (2026-ANCHOR-01-016-01).

References

1. Kisseleva T, Brenner D. Molecular and cellular mechanisms of liver fibrosis and its regression. Nat Rev Gastroenterol Hepatol. 2021; 18: 151–66.

2. Sharma S, Le Guillou D, Chen JY. Cellular stress in the pathogenesis of nonalcoholic steatohepatitis and liver fibrosis. Nat Rev Gastroenterol Hepatol. 2023; 20: 662–78.

3. Kisseleva T, Ganguly S, Murad R, Wang A, Brenner DA. Regulation of Hepatic Stellate Cell Phenotypes in Metabolic Dysfunction-Associated Steatohepatitis. Gastroenterology. 2025.

4. Huang DQ, Terrault NA, Tacke F, Gluud LL, Arrese M, Bugianesi E, et al. Global epidemiology of cirrhosis - aetiology, trends and predictions. Nat Rev Gastroenterol Hepatol. 2023; 20: 388–98.

5. Shetty S, Lalor PF, Adams DH. Liver sinusoidal endothelial cells - gatekeepers of hepatic immunity. Nat Rev Gastroenterol Hepatol. 2018; 15: 555–67.

6. Gracia-Sancho J, Caparrós E, Fernández-Iglesias A, Francés R. Role of liver sinusoidal endothelial cells in liver diseases. Nat Rev Gastroenterol Hepatol. 2021; 18: 411–31.

7. Qu J, Wang L, Li Y, Li X. Liver sinusoidal endothelial cell: An important yet often overlooked player in the liver fibrosis. Clin Mol Hepatol. 2024; 30: 303–25.

8. Gao J, Lan T, Kostallari E, Guo Y, Lai E, Guillot A, et al. Angiocrine signaling in sinusoidal homeostasis and liver diseases. J Hepatol. 2024; 81: 543–61.

9. Unterholzner L, Keating SE, Baran M, Horan KA, Jensen SB, Sharma S, et al. IFI16 is an innate immune sensor for intracellular DNA. Nat Immunol. 2010; 11: 997–1004.

10. Choubey D, Panchanathan R. IFI16, an amplifier of DNA-damage response: Role in cellular senescence and aging-associated inflammatory diseases. Ageing Res Rev. 2016; 28: 27–36.

11. Dunphy G, Flannery SM, Almine JF, Connolly DJ, Paulus C, Jønsson KL, et al. Non-canonical Activation of the DNA Sensing Adaptor STING by ATM and IFI16 Mediates NF-κB Signaling after Nuclear DNA Damage. Mol Cell. 2018; 71: 745–60.e5.

12. Ka NL, Lim GY, Hwang S, Kim SS, Lee MO. IFI16 inhibits DNA repair that potentiates type-I interferon-induced antitumor effects in triple negative breast cancer. Cell Rep. 2021; 37: 110138.

13. Yu Y, Liu Y, An W, Song J, Zhang Y, Zhao X. STING-mediated inflammation in Kupffer cells contributes to progression of nonalcoholic steatohepatitis. J Clin Invest. 2019; 129: 546–55.

14. Arumugam S, Li B, Boodapati SLT, Nathanson MH, Sun B, Ouyang X, et al. Mitochondrial DNA and the STING pathway are required for hepatic stellate cell activation. Hepatology. 2023; 78: 1448–61.

15. Kim D, Shah M, Kim JH, Kim J, Baek YH, Jeong JS, et al. Integrative transcriptomic and genomic analyses unveil the IFI16 variants and expression as MASLD progression markers. Hepatology. 2025; 81: 962–75.

16. Lim GY, Cho SW, Ka NL, Lee KH, Im SA, Kim SS, et al. IFI16/Ifi202 released from breast cancer induces secretion of inflammatory cytokines from macrophages and promotes tumor growth. J Cell Physiol. 2023; 238: 1507–19.

17. Alunno A, Caneparo V, Carubbi F, Bistoni O, Caterbi S, Gariglio M, et al. Interferon gamma-inducible protein 16 (IFI16) and anti-IFI16 antibodies in primary Sjögren's syndrome: findings in serum and minor salivary glands. Reumatismo. 2015; 67: 85–90.

18. Alunno A, Caneparo V, Bistoni O, Caterbi S, Terenzi R, Gariglio M, et al. Circulating Interferon-Inducible Protein IFI16 Correlates With Clinical and Serological Features in Rheumatoid Arthritis. Arthritis Care Res (Hoboken). 2016; 68: 440–5.

19. Gugliesi F, Bawadekar M, De Andrea M, Dell'Oste V, Caneparo V, Tincani A, et al. Nuclear DNA sensor IFI16 as circulating protein in autoimmune diseases is a signal of damage that impairs endothelial cells through high-affinity membrane binding. PLoS One. 2013; 8: e63045.

20. Iannucci A, Caneparo V, Raviola S, Debernardi I, Colangelo D, Miggiano R, et al. Toll-like receptor 4-mediated inflammation triggered by extracellular IFI16 is enhanced by lipopolysaccharide binding. PLoS Pathog. 2020; 16: e1008811.

21. Kim HJ, Jeong C, Lee SH, An S, Hyun GH, Lim GY, et al. LncRNA Wee1-AS coordinates oxidative fatty acid metabolism through the activation of mitochondrial CDK1/CYCLIN B1. Signal Transduct Target Ther. 2026; 11: 13.

22. Korsunsky I, Millard N, Fan J, Slowikowski K, Zhang F, Wei K, et al. Fast, sensitive and accurate integration of single-cell data with Harmony. Nat Methods. 2019; 16: 1289–96.

23. Franzén O, Gan LM, Björkegren JLM. PanglaoDB: a web server for exploration of mouse and human single-cell RNA sequencing data. Database (Oxford). 2019; 2019.

24. Ojha U, Kim S, Rhee CY, You J, Choi YH, Yoon SH, et al. Endothelial RUNX3 controls LSEC dysfunction and angiocrine LRG1 signaling to prevent liver fibrosis. Hepatology. 2025; 81: 1228–43.

25. Kim HJ, Han YH, Na H, Kim JY, Kim T, Kim HJ, et al. Liver-specific deletion of RORα aggravates diet-induced nonalcoholic steatohepatitis by inducing mitochondrial dysfunction. Sci Rep. 2017; 7: 16041.

26. Kim HY, Lee W, Liu X, Jang H, Sakane S, Carvalho-Gontijo Weber R, et al. Protocol to generate human liver spheroids to study liver fibrosis induced by metabolic stress. STAR Protoc. 2024; 5: 103111.

27. Han YH, Kim HJ, Kim EJ, Kim KS, Hong S, Park HG, et al. RORα decreases oxidative stress through the induction of SOD2 and GPx1 expression and thereby protects against nonalcoholic steatohepatitis in mice. Antioxid Redox Signal. 2014; 21: 2083–94.

28. Fan X, Jiao L, Jin T. Activation and Immune Regulation Mechanisms of PYHIN Family During Microbial Infection. Front Microbiol. 2021; 12: 809412.

29. Su T, Yang Y, Lai S, Jeong J, Jung Y, McConnell M, et al. Single-Cell Transcriptomics Reveals Zone-Specific Alterations of Liver Sinusoidal Endothelial Cells in Cirrhosis. Cell Mol Gastroenterol Hepatol. 2021; 11: 1139–61.

30. Schwabe RF, Brenner DA. Hepatic stellate cells: balancing homeostasis, hepatoprotection and fibrogenesis in health and disease. Nat Rev Gastroenterol Hepatol. 2025; 22: 481–99.

31. Volchuk A, Ye A, Chi L, Steinberg BE, Goldenberg NM. Indirect regulation of HMGB1 release by gasdermin D. Nat Commun. 2020; 11: 4561.

32. Wang J, Shen Z, Chen G, Dai W, Mei Z, Shen B, et al. YAP contributes to liver injury through mediating capillarization of liver sinusoidal endothelial cells via GATA6/eNOS signaling. Cell Mol Biol Lett. 2025; 30: 119.

33. Fernández-Duran I, Quintanilla A, Tarrats N, Birch J, Hari P, Millar FR, et al. Cytoplasmic innate immune sensing by the caspase-4 non-canonical inflammasome promotes cellular senescence. Cell Death Differ. 2022; 29: 1267–82.

34. Getachew A, Hussain M, Huang X, Li Y. Toll-like receptor 2 signaling in liver pathophysiology. Life Sci. 2021; 284: 119941.

35. Zheng M, Karki R, Williams EP, Yang D, Fitzpatrick E, Vogel P, et al. TLR2 senses the SARS-CoV-2 envelope protein to produce inflammatory cytokines. Nat Immunol. 2021; 22: 829–38.

36. Kim HY, Rosenthal SB, Liu X, Miciano C, Hou X, Miller M, et al. Multi-modal analysis of human hepatic stellate cells identifies novel therapeutic targets for metabolic dysfunction-associated steatotic liver disease. J Hepatol. 2025; 82: 882–97.

37. Bhandari S, Kyrrestad I, Simón-Santamaría J, Li R, Szafranska KJ, Dumitriu G, et al. Mouse liver sinusoidal endothelial cell responses to the glucocorticoid receptor agonist dexamethasone. Front Pharmacol. 2024; 15: 1377136.

38. Lefere S, Van de Velde F, Hoorens A, Raevens S, Van Campenhout S, Vandierendonck A, et al. Angiopoietin-2 Promotes Pathological Angiogenesis and Is a Therapeutic Target in Murine Nonalcoholic Fatty Liver Disease. Hepatology. 2019; 69: 1087–104.

39. Wu X, Shu L, Zhang Z, Li J, Zong J, Cheong LY, et al. Adipocyte Fatty Acid Binding Protein Promotes the Onset and Progression of Liver Fibrosis via Mediating the Crosstalk between Liver Sinusoidal Endothelial Cells and Hepatic Stellate Cells. Adv Sci (Weinh). 2021; 8: e2003721.

40. Chen Z, Behrendt R, Wild L, Schlee M, Bode C. Cytosolic nucleic acid sensing as driver of critical illness: mechanisms and advances in therapy. Signal Transduct Target Ther. 2025; 10: 90.

41. Hong Q, Cai H, Zhang L, Li Z, Zhong F, Ni Z, et al. Modulation of transforming growth factor-β-induced kidney fibrosis by leucine-rich α-2 glycoprotein-1. Kidney Int. 2022; 101: 299–314.

42. Urushima H, Fujimoto M, Mishima T, Ohkawara T, Honda H, Lee H, et al. Leucine-rich alpha 2 glycoprotein promotes Th17 differentiation and collagen-induced arthritis in mice through enhancement of TGF-β-Smad2 signaling in naïve helper T cells. Arthritis Res Ther. 2017; 19: 137.

43. Hahn A, Kny M, Pablo-Tortola C, Todiras M, Willenbrock M, Schmidt S, et al. Serum amyloid A1 mediates myotube atrophy via Toll-like receptors. J Cachexia Sarcopenia Muscle. 2020; 11: 103–19.

44. Chowdhary VR, Crowson CS, Poterucha JJ, Moder KG. Liver involvement in systemic lupus erythematosus: case review of 40 patients. J Rheumatol. 2008; 35: 2159–64.

45. Guo Z, Wu D, Mao R, Yao Z, Wu Q, Lv W. Global burden of MAFLD, MAFLD related cirrhosis and MASH related liver cancer from 1990 to 2021. Sci Rep. 2025; 15: 7083.

46. Rinella ME, Sookoian S. Therapeutic targets for metabolic dysfunction-associated steatohepatitis: a personalized approach to disease management. Nat Rev Gastroenterol Hepatol. 2026; 23: 460–74.

47. Peng D, Fu M, Wang M, Wei Y, Wei X. Targeting TGF-β signal transduction for fibrosis and cancer therapy. Mol Cancer. 2022; 21: 104.

48. Deng Z, Fan T, Xiao C, Tian H, Zheng Y, Li C, et al. TGF-β signaling in health, disease, and therapeutics. Signal Transduct Target Ther. 2024; 9: 61.

Figures

Figure 1. Lim et al

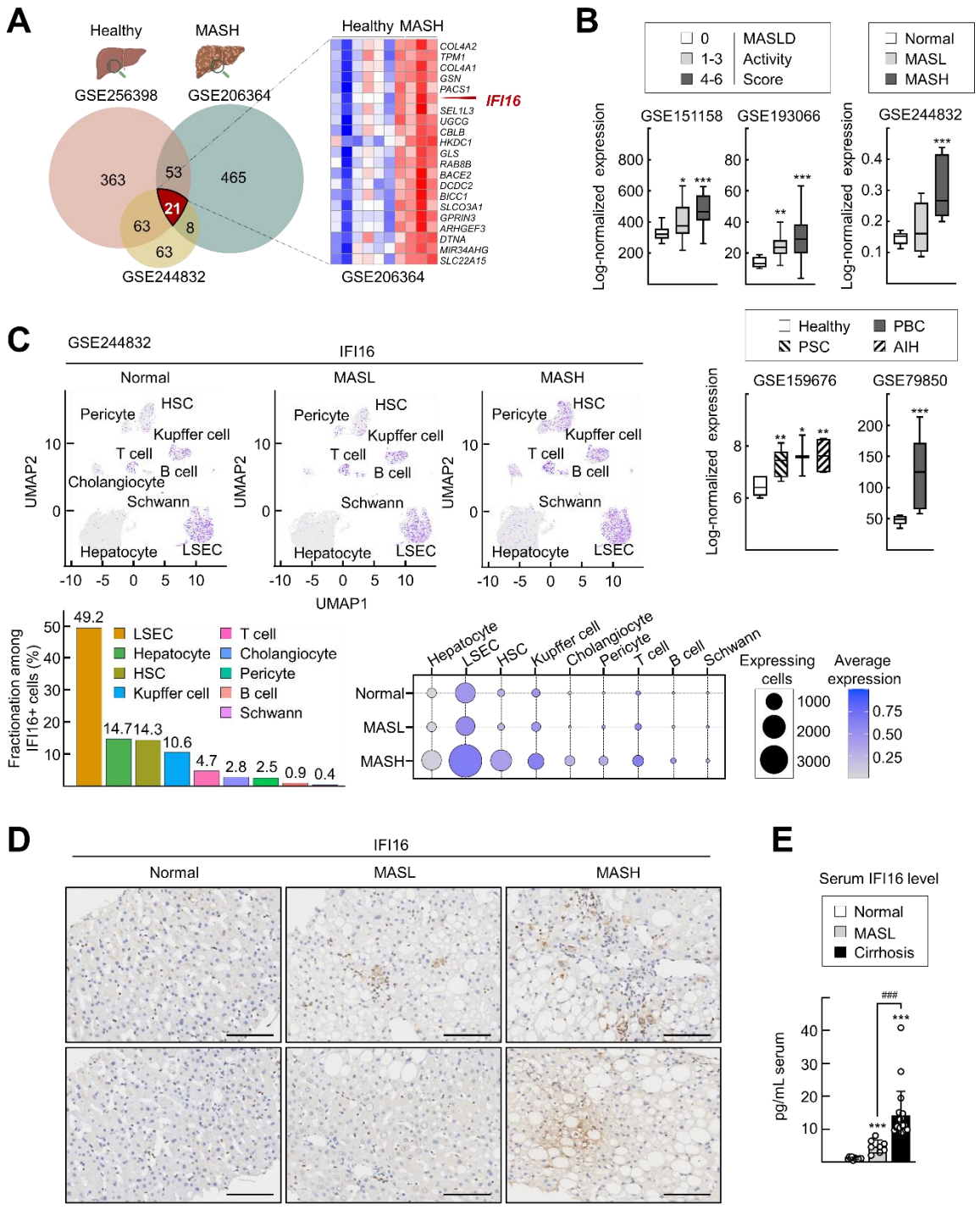


Figure 1. Hepatic and circulating levels of human IFI16 are elevated during progression of MASLD.

(A) Differential expression analysis was performed using bulk transcriptomic datasets (GSE256398, GSE206364, and GSE244832). A total of 21 genes were commonly upregulated (log_2fold-change > 0.5, $p < 0.0001$; DESeq2), with a representative heatmap of these genes shown. Sample sizes were as follows: GSE256398, Healthy (*n = 6*) and MASH (*n = 8*); GSE206364, Healthy (*n = 7*) and Cirrhosis (*n = 3*); GSE244832, Normal (*n = 5*) and MASH (*n = 9*). Expression values were normalized by Z-score. **(B)** *IFI16* mRNA levels were analyzed in public datasets (GSE151158, GSE193066, GSE244832, GSE159676, and GSE79850), comparing patients with various liver diseases—including MASLD, PBC, PSC, AIH, and MASH—to healthy individuals or those with a MASLD (previously classified as NAFLD) activity score of 0. GSE151158: 0 (*n = 21*), 1–3 (*n = 23*), 4–6 (*n = 17*); GSE193066: 0 (*n = 4*), 1–3 (*n = 81*), 4–6 (*n = 79*); GSE244832: Normal (*n = 5*), MASL (*n = 4*), MASH (*n = 9*); GSE159676: Healthy (*n = 7*), PSC (*n = 11*), PBC (*n = 3*), AIH (*n = 4*); GSE79850: Healthy (*n = 8*), PBC (*n = 9*). Box-and-whisker plots show the median (line within the box), the interquartile range (bounds of the box), and whiskers extending to values within 1.5 × IQR (Tukey method). Outliers beyond this range are shown as individual dots. Statistical significance was assessed using the two-tailed Mann–Whitney *U* test (n values as indicated above). All data are shown as mean ± SD, $^{*}P < 0.05$, $^{**}P < 0.01$, $^{***}P < 0.001$ *vs* healthy controls or MASLD activity score 0 (GSE151158 and GSE193066). **(C)** Single-nucleus RNA sequencing data (GSE244832; *n = 18* individuals with varying MASLD stages) were analyzed to visualize IFI16 expression across liver cell populations (top). The UMAP plot shows clustering of hepatic cell populations. IFI16-positive cell population was quantitatively analyzed (bottom left). The dot plot depicts normalized IFI16 expression across these clusters, with a gray-to-blue gradient indicating relative expression (Z-score) (bottom right). **(D)** Representative immunohistochemistry of IFI16 in human liver tissues from normal, MASL, and MASH patients. Scale bar, 100 μm. **(E)** Serum level of human IFI16 quantified using ELISA in normal individuals (*n = 11*), MASL (*n = 8*), and cirrhosis (*n = 21*). Data are shown as mean ± SEM. $^{***}P < 0.001$ *vs* Normal, $^{###}P < 0.001$ *vs* MASL. Statistical significance was assessed using the two-tailed Mann–Whitney *U* test.

Abbreviations: AIH, autoimmune hepatitis; PBC, primary biliary cholangitis; PSC, primary sclerosing cholangitis.

Figure 2. Lim et al

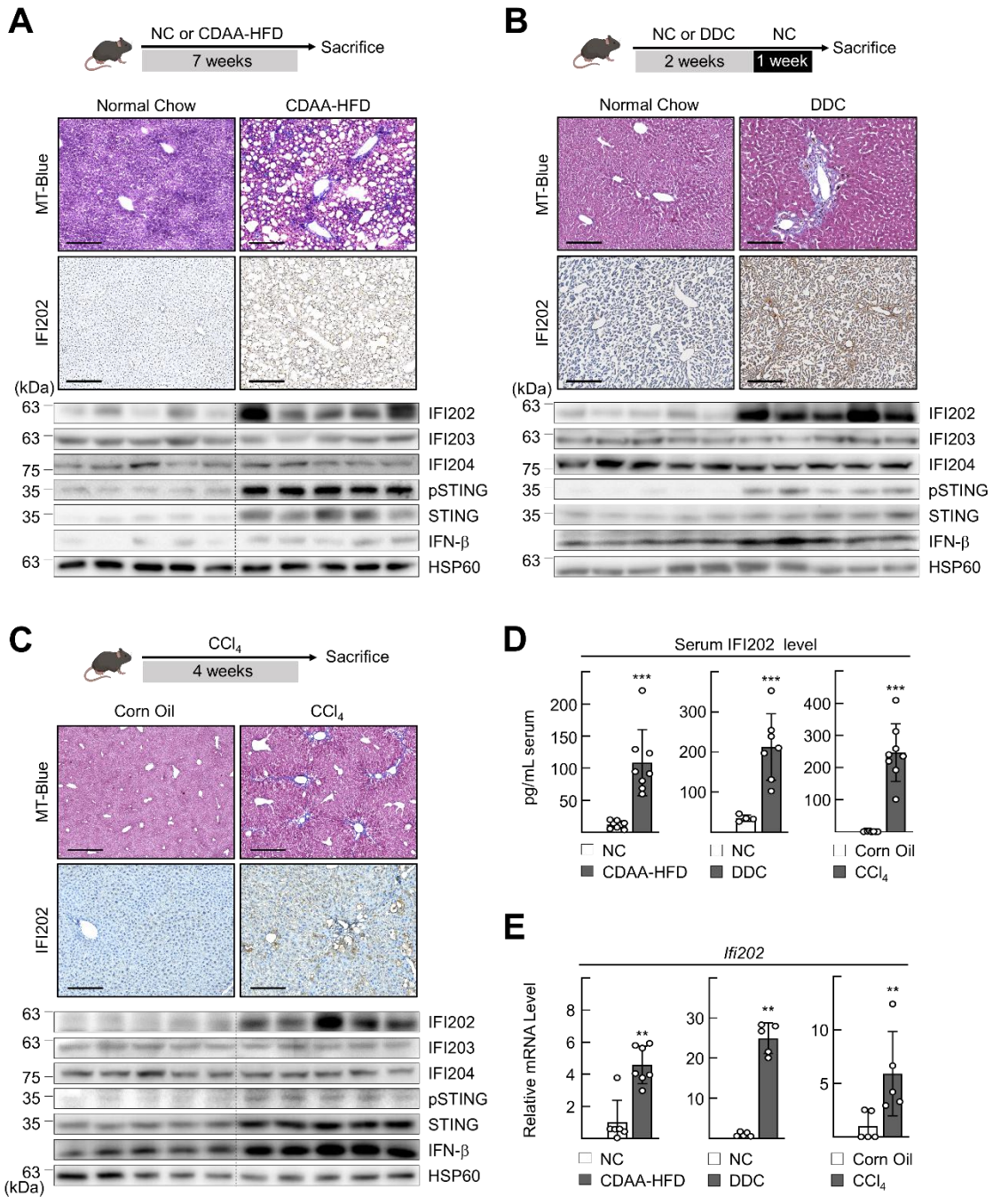
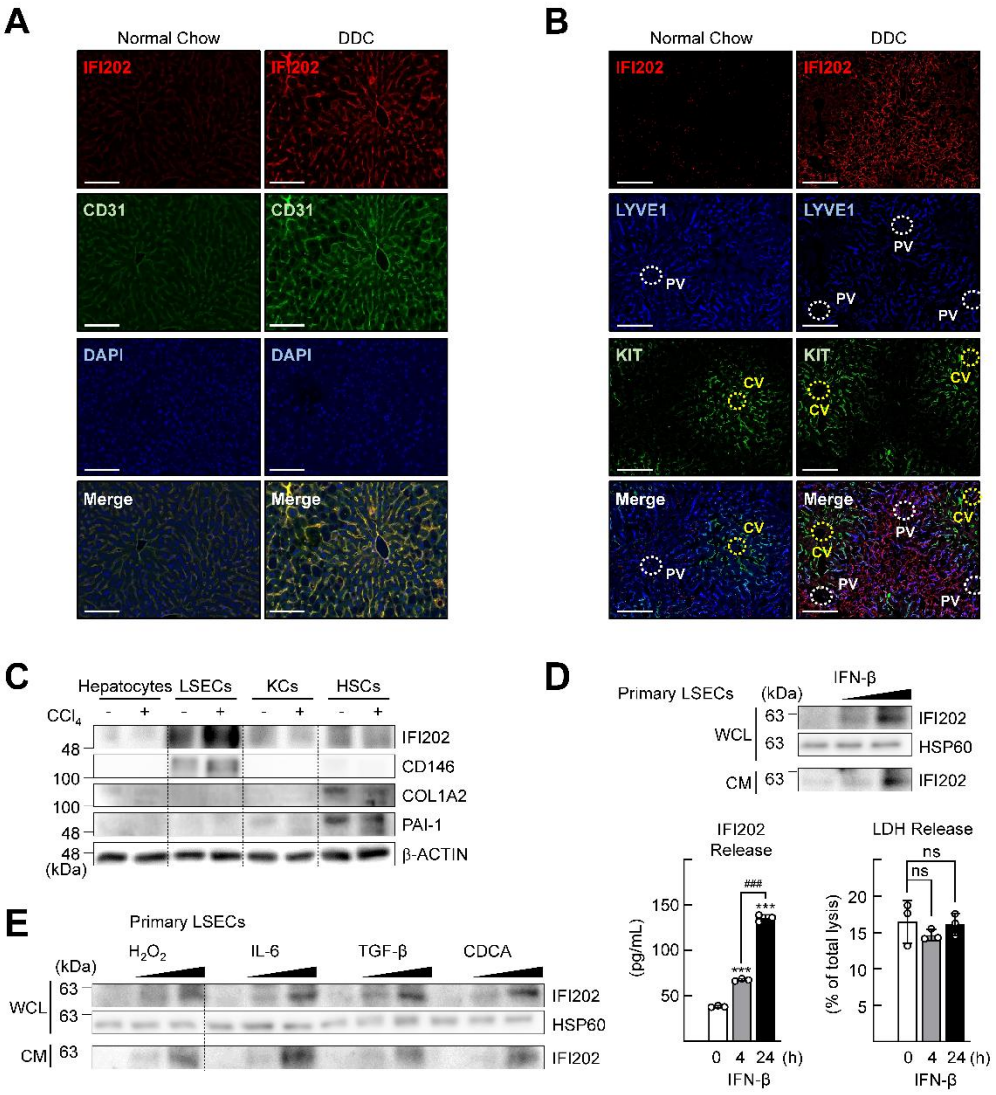


Figure 2. IFI202 levels in the liver and the serum are increased after fibrosis-inducing liver injury in mice.

(A) Eight-week-old male mice were fed a CDAA-HFD (*n = 8*) or normal chow (NC; *n = 8*) for 7 weeks. Masson's trichrome and IFI202 immunohistochemistry of liver sections are shown (top). Scale bar, 200 μm. Hepatic expression of IFI202, IFI203, IFI204, pSTING, STING, and IFN-β was analyzed by western blot (bottom). **(B)** Seven-week-old male mice were fed a 0.1% DDC diet (*n = 7*) or NC (*n = 4*) for 2 weeks, followed by 1 week on NC. Masson's trichrome and IFI202 immunohistochemistry of liver sections are shown (top). Scale bar, 200 μm. Hepatic expression of IFI202, IFI203, IFI204, pSTING, STING, and IFN-β was analyzed by western blot (bottom). **(C)** Seven-week-old male mice received intraperitoneal injections of CCl_4 (*n = 8*; 50 μL/100 g body weight) or corn oil (*n = 5*) twice weekly for 4 weeks. Masson's trichrome and IFI202 immunohistochemistry of liver sections are shown (top). Scale bar, 200 μm. Hepatic expression of IFI202, IFI203, IFI204, pSTING, STING, and IFN-β was analyzed by western blot (bottom). **(D**) Serum IFI202 levels were measured by ELISA in NC (*n = 8*) and CDAA-HFD (*n = 8*) groups (left). $^{***}P < 0.001$ *vs* NC. Serum IFI202 levels were measured by ELISA in NC (*n = 4*) and DDC (*n = 7*) groups (middle). $^{***}P < 0.001$ *vs* NC. Serum IFI202 levels were measured by ELISA in corn oil (*n = 5*) and CCl_4 (*n = 8*) groups (right). $^{***}P < 0.001$ *vs* corn oil. (**E**) Liver tissue *Ifi202* mRNA levels were measured by qPCR in NC (*n = 6*) and CDAA-HFD (*n = 7*) groups (left), NC (*n = 5*) and DDC (*n = 5*) groups (middle), and corn oil (*n = 5*) and CCl_4 (*n = 5*) groups (right). $^{**}P < 0.01$ *vs* NC or corn oil. All data are presented as mean ± SD. Statistical significance was determined using the two-tailed Mann–Whitney *U* test.

Abbreviations: IFI202, interferon-inducible protein 202; IFI203, interferon-inducible protein 203; IFI204, interferon-inducible protein 204; NC, normal chow; pSTING, phosphorylated stimulator of interferon genes.

Figure 3. Lim et al



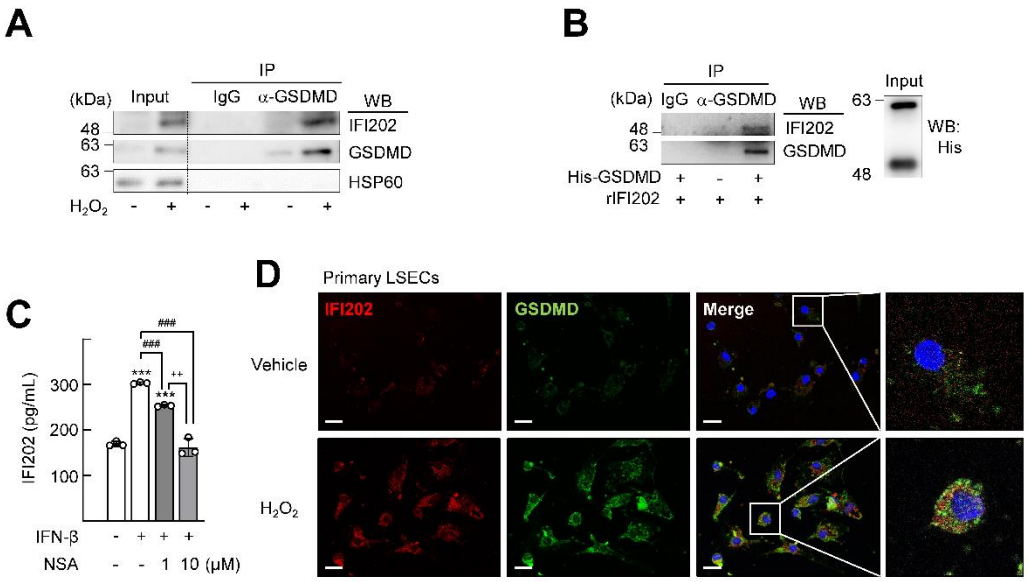
1

Figure 3. IFI202 is secreted from the LSECs under cellular stress.

(A, B) Representative immunofluorescence images of liver sections from mice fed a normal chow or 0.1% DDC diet. IFI202 (red), CD31 (green), and merged images (**A**). IFI202 (red), LYVE1 (blue), KIT (green), and merged images (**B**). Scale bar, 100 μm. (**C**) Western blot analysis of IFI202 expression in primary hepatocytes, LSECs, KCs, and HSCs from mice treated with CCl_4 (50 μL/100 g body weight) or corn oil, collected 48 h after injection. CD146 was used as a marker for LSECs, COL1A2 and PAI-1 for HSCs, and β-ACTIN as the loading control. **(D)** Primary LSECs were seeded at 1×10^6 cells/well and treated with IFN-β (0, 0.2, 2 ng/mL). WCL and CM were analyzed by western blot for IFI202 expression and secretion (top). LSECs were treated with IFN-β (10 ng/mL) for 0, 4, or 24 h. CM was collected, and IFI202 concentrations were measured by ELISA (bottom, left). LDH release was quantified in culture media collected under the same conditions and normalized to Tergitol-induced total lysis, which served as the positive control and was defined as 100% maximal LDH release (bottom, right). Data are presented as mean ± SD ($n = 3$). Statistical significance was determined by unpaired *t*-test. $^{***}P < 0.001$ *vs* 0 h, $^{\#\#\#}P < 0.001$ *vs* 4 h. ns, not significant. **(E)** LSECs were treated for 24 h with H_2O_2 (0, 10, 100 nM), IL-6 (0, 0.2, 2 μg/mL), TGF-β (0, 2, 10 ng/mL) or CDCA (0, 20, 200 μM). WCL and CM were analyzed by western blot for IFI202 expression and secretion.

Abbreviations: CM, conditioned medium; IFI202, interferon-inducible protein 202; PAI-1, plasminogen activator inhibitor-1; WCL, whole cell lysate.

Figure 4. Lim et al



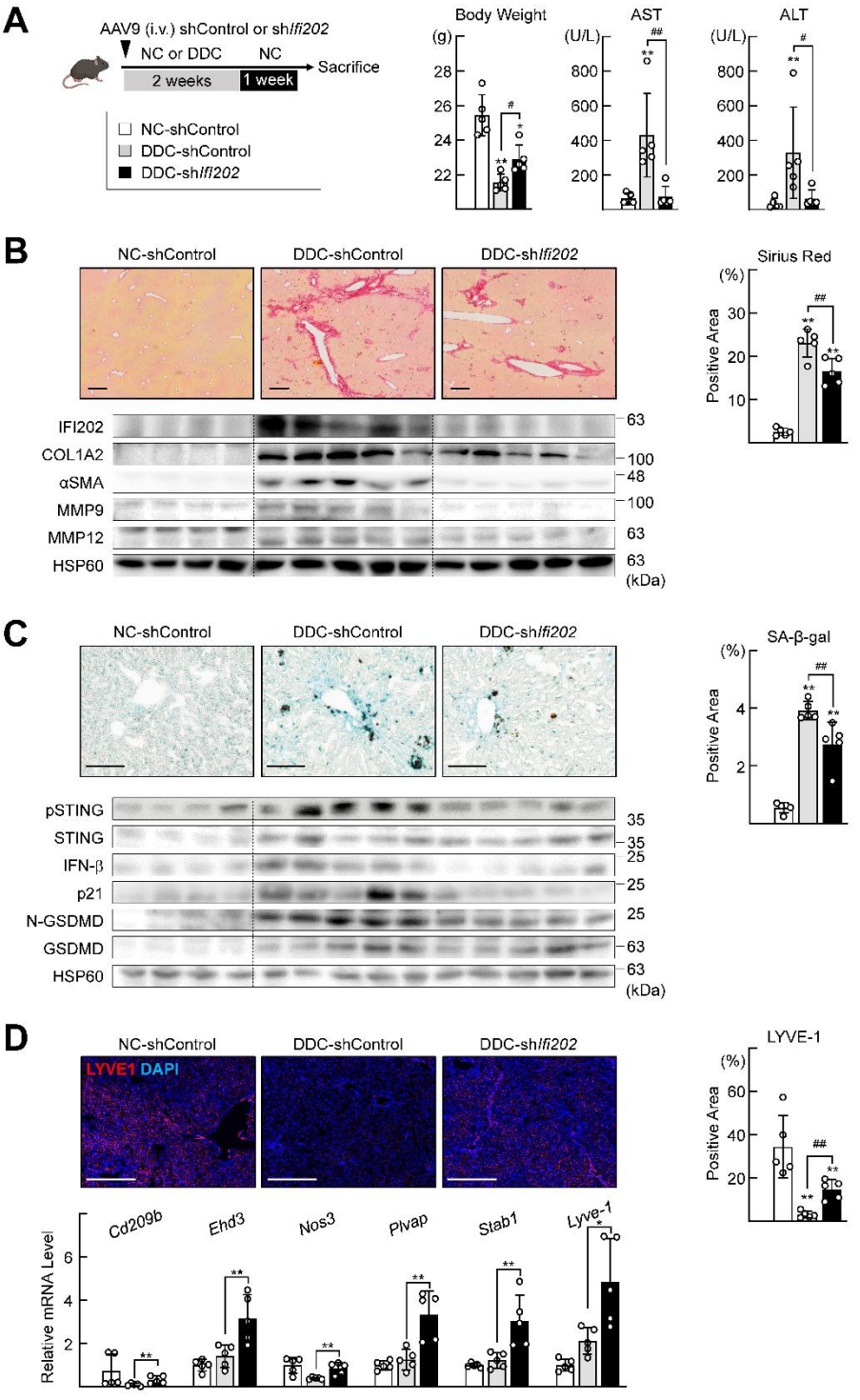
1

Figure 4. IFI202 is secreted *via* the pore-forming protein gasdermin D in LSECs

(A) EOMA cells treated with H_2O_2 (100 nM, 24 h) were subjected to GSDMD immunoprecipitation followed by western blot. Predicted interaction between GSDMD and IFI202 by AlphaFold2 (mean ipTM score = 0.344). **(B)** Recombinant His-tagged GSDMD (aa 1–325) and recombinant His-tagged IFI202 proteins, alone or in combination, were subjected to immunoprecipitation with an anti-GSDMD antibody or control IgG, followed by western blotting with indicated antibodies. Western blotting with anti-His antibody showed two His-tagged protein bands as input. **(C)** Primary LSECs were treated with IFN-β (0.2 ng/mL) and necrosulfonamide (NSA; 1 or 10 μM) for 24 h. CM was collected, and IFI202 concentrations were measured by ELISA. Data are presented as mean ± SD (*n = 3*). Statistical significance was determined by unpaired *t*-test. $^{***}P < 0.001$ *vs* IFN-β (0 ng/mL) + NSA (0 μM); $^{\#\#\#}P < 0.001$ *vs* IFN-β (0.2 ng/mL) + NSA (0 μM); $^{++}P < 0.01$ *vs* IFN-β (0.2 ng/mL) + NSA (1 μM). **(D)** Primary LSECs treated with H_2O_2 (100 nM, 4 h) were analyzed by immunofluorescence for GSDMD and IFI202 expression and co-localization. Scale bar, 10 μm.

Abbreviations: CM, conditioned medium; GSDMD, gasdermin D; IFI202, interferon-inducible protein 202; NSA, necrosulfonamide; WCL, whole cell lysate.

Figure 5. Lim et al



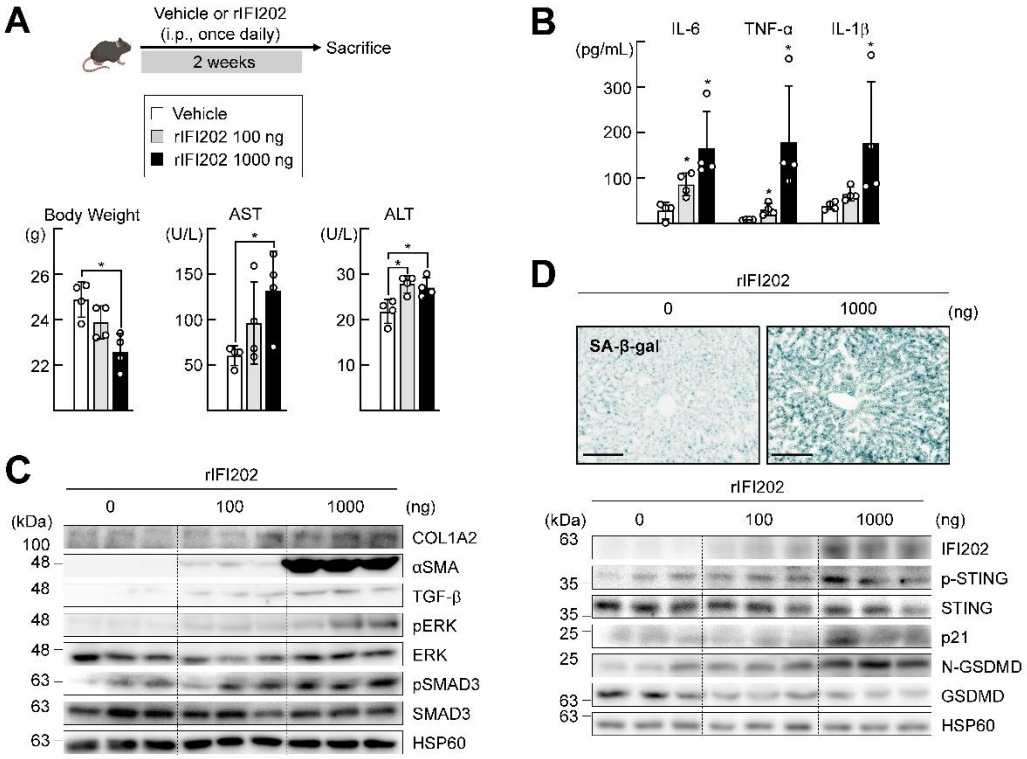
1

Figure 5. Knockdown of *Ifi202* alleviates DDC diet-induced fibrosis.

(A) Experimental design (left). Mice were fed NC, 0.1% DDC diet with shControl, or a 0.1% DDC diet with shRNA-mediated *Ifi202* knockdown (sh*Ifi202*). Body weight and serum AST and ALT levels were measured (right). **(B)** Sirius Red staining of liver sections showing collagen deposition (left; scale bar, 1 mm) with quantification (right), and western blot analysis of IFI202, COL1A2, αSMA, MMP9, MMP12, and HSP60 as loading control. **(C)** SA-β-gal staining of liver sections (left; scale bar, 100 μm) with quantification (right), and western blot of pSTING, STING, IFN-β, p21, N-GSDMD, and GSDMD in liver tissues. **(D)** Immunofluorescence staining of LYVE1 (red) with DAPI (blue) in liver sections (scale bar, 100 μm) with quantification (right), and qRT-PCR analysis of vascular function-related genes (*Cd209b, Ehd3, Nos3, Plvap, Stab1, Lyve1*). All Data are presented as mean ± SD (*n = 5* per group), except for the western blot analyses, which were performed using *n = 4, 5, and 5* biological samples for the NC-shControl, DDC-shControl, and DDC-sh*Ifi202* groups, respectively. Statistical analyses were performed using the two-tailed Mann–Whitney *U* test. $^{**}P < 0.01$, $^{*}P < 0.05$ *vs* NC-shControl; $^{\#\#}P < 0.01$, $^{\#}P < 0.05$ *vs* DDC-shControl.

Abbreviations: GSDMD, gasdermin D; HSP60, heat shock protein 60; LYVE1, lymphatic vessel endothelial hyaluronan receptor 1; MMP12, matrix metalloproteinase 12; MMP9, matrix metalloproteinase 9; NC, normal chow; pSTING, phosphorylated stimulator of interferon genes; SA-β-gal, senescence-associated beta-galactosidase.

Figure 6. Lim et al



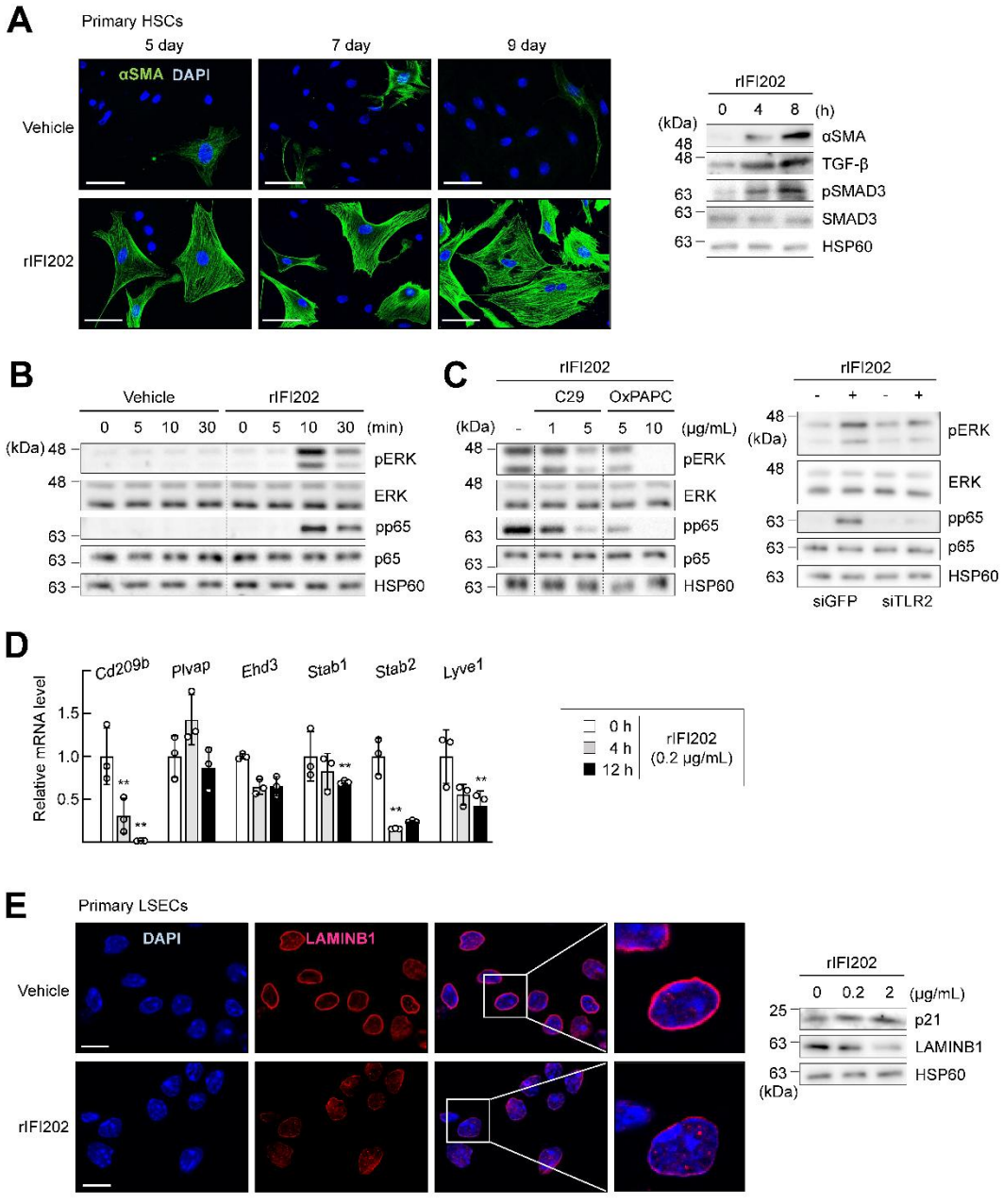
1

Figure 6. Injection of IFI202 induces fibrotic changes in the liver.

(A) Experimental design (top). Eight-week-old male mice were injected intraperitoneally with rIFI202 protein (100 or 1000 ng daily) for 2 weeks. Body weight and serum AST and ALT levels were measured (bottom). **(B)** Serum IL-6, TNF-α, and IL-1β levels measured by ELISA. **(C)** Western blot of COL1A2, αSMA, TGF-β, pERK, and pSMAD3, with ERK, SMAD3, and HSP60 as controls. **(D)** SA-β-galactosidase staining of liver sections (top, scale bar, 100 μm) and western blot of IFI202, pSTING, STING, p21, N-GSDMD and GSDMD in liver tissues (bottom). All data are shown as mean ± SD (*n* = *4* per group). Statistical significance was determined using the two-tailed Mann–Whitney *U* test. $^{*}P < 0.05$ *vs* vehicle.

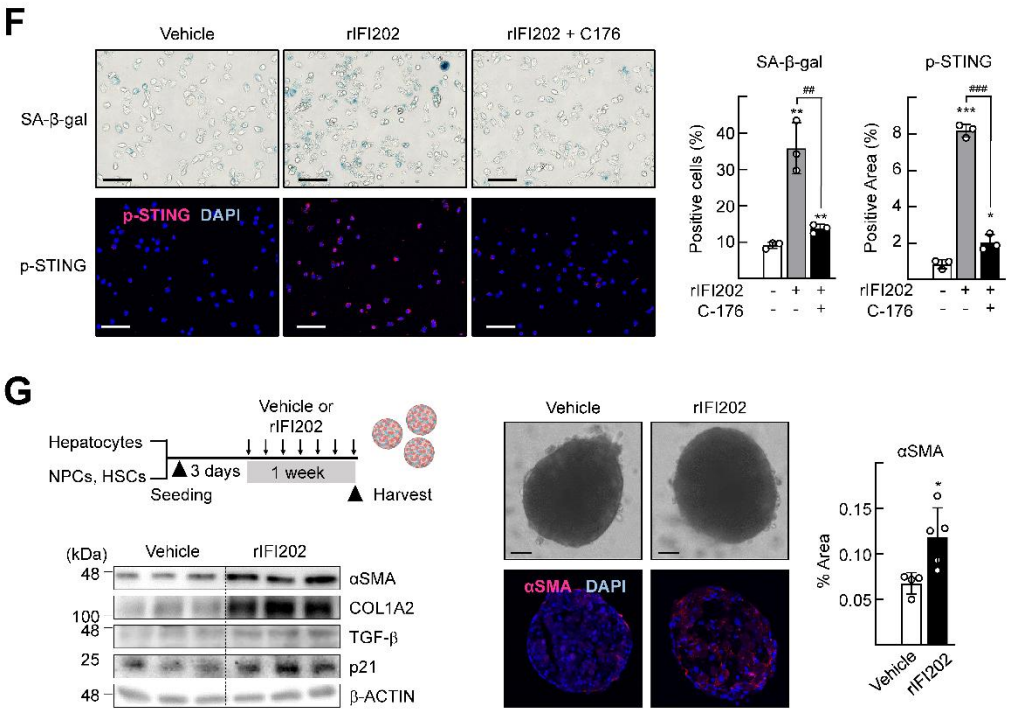
Abbreviations: HSP60, heat shock protein 60; pERK, phosphorylated extracellular signal–regulated kinase; pSMAD3, phosphorylated SMAD family member 3; pSTING, phosphorylated stimulator of interferon genes; SA-β-gal, senescence-associated beta-galactosidase.

Figure 7. Lim et al



1

Figure 7. Lim et al (cont'd)



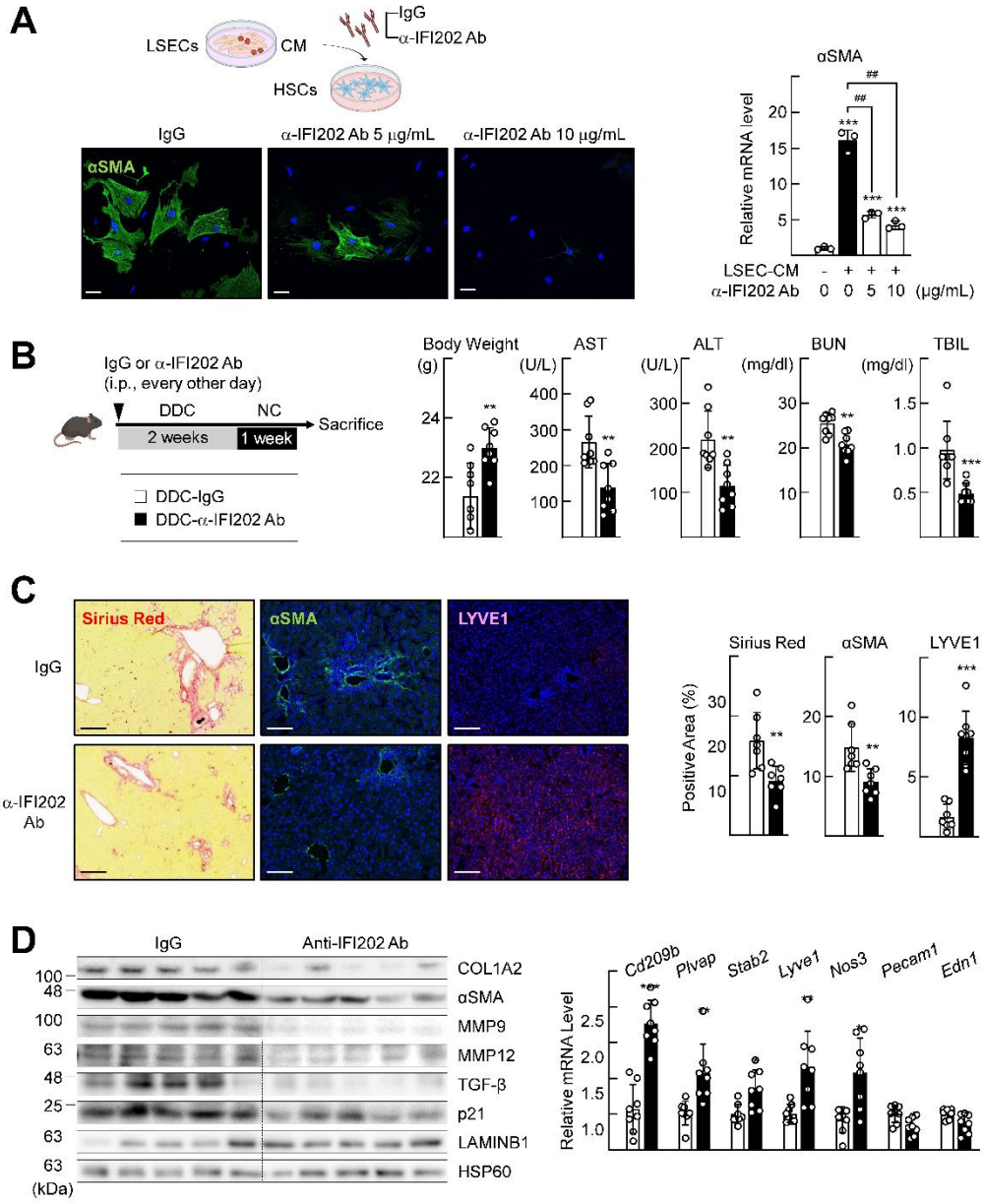
1

Figure 7. IFI202 induces activation in HSCs and cellular senescence in LSECs.

(A) Primary HSCs were seeded at 1 × 10^6 cells/well and treated daily with rIFI202 (0.2 μg/mL) or vehicle beginning 1 day after seeding. Immunofluorescence staining for αSMA (green) with DAPI nuclear counterstain (blue) was performed on days 5, 7, and 9 (left; scale bar, 50 μm). HSCs cultured for 7 days were then treated with rIFI202 (0.2 μg/mL) for 0, 4, or 8 h, and expression of αSMA, TGF-β, pSMAD3, and SMAD3 was analyzed by western blot (right). **(B**) Primary HSCs were seeded at 1 × 10^6 cells/well and, after 2 days of culture, treated with rIFI202 (0.2 μg/mL) or vehicle for 0, 5, 10, and 30 min. The expression levels of pERK, ERK, pp65 and p65 were then analyzed by western blot. (**C**) Primary HSCs were seeded at 1 × 10^6 cells/well and cultured for 2 days, then preincubated for 1 h with TLR2 inhibitors (C29 at 1 and 5 μg/mL or OxPAPC at 5 and 10 μg/mL) followed by treatment with rIFI202 (0.2 μg/mL) for 10 min (left). Primary HSCs were transfected with si-GFP or si-TLR2 for 48 h and subsequently treated with rIFI202 (0.2 μg/mL) for 10 min. The expression levels of p-ERK/ERK, p-p65/p65, and TLR2 were then analyzed by western blotting (right). (**D**) Expression of vascular function-related genes (*Cd209b, Plvap, Ehd3, Nos3, Stab1, Stab2, Lyve1*) was measured by qRT-PCR in LSECs treated with rIFI202 (0.2 μg/mL) or vehicle. Data are shown as mean ± SD (*n = 3*). Statistical significance was determined using unpaired *t*-test. $^{**}P < 0.01$ *vs* 0 h. **(E)** Primary LSECs were seeded at 0.5 × 10^6 cells/well and treated with rIFI202 (0.2 μg/mL, 4 h) or vehicle. Immunofluorescence staining for LAMIN B1 was performed (left; scale bar, 10 μm). Expression of p21 and LAMIN B1 was assessed by western blot (right). **(F)** Primary LSECs were seeded at 0.5 × 10^6 cells/well and treated with rIFI202 (2 μg/mL) or vehicle for 4 h. C-176 (1 μM) was pretreated for 1 h before rIFI202 (2 μg/mL) treatment. SA-β-gal staining and immunofluorescence staining for p-STING were performed (scale bar, 50 μm). SA-β-gal-positive cells were counted and represented as a percentage of the total cells. p-STING-positive area was quantified using image J. Data are presented as mean ± SD (*n = 3*). Statistical significance was determined by unpaired *t*-test. $^{*}P < 0.05$, $^{**}P < 0.01$, $^{***}P < 0.001$ *vs* vehicle; $^{\#\#}P < 0.01$, $^{\#\#\#}P < 0.001$ *vs* rIFI202. **(G)** Mouse liver spheroids were treated from day 3 for 7 days with rIFI202 (0.2 μg/mL) or vehicle. On day 10, expression of αSMA, COL1A2, TGF-β, and p21 was analyzed by western blot (left). Spheroids were imaged by light microscopy and stained for αSMA by immunofluorescence, with quantification shown (right, scale bar, 100 μm). Data are shown as mean ± SD (*n = 4* for vehicle, *n = 5* for rIFI202). Statistical significance was determined using the two-tailed Mann–Whitney *U* test. $^{*}P < 0.05$ *vs* vehicle.

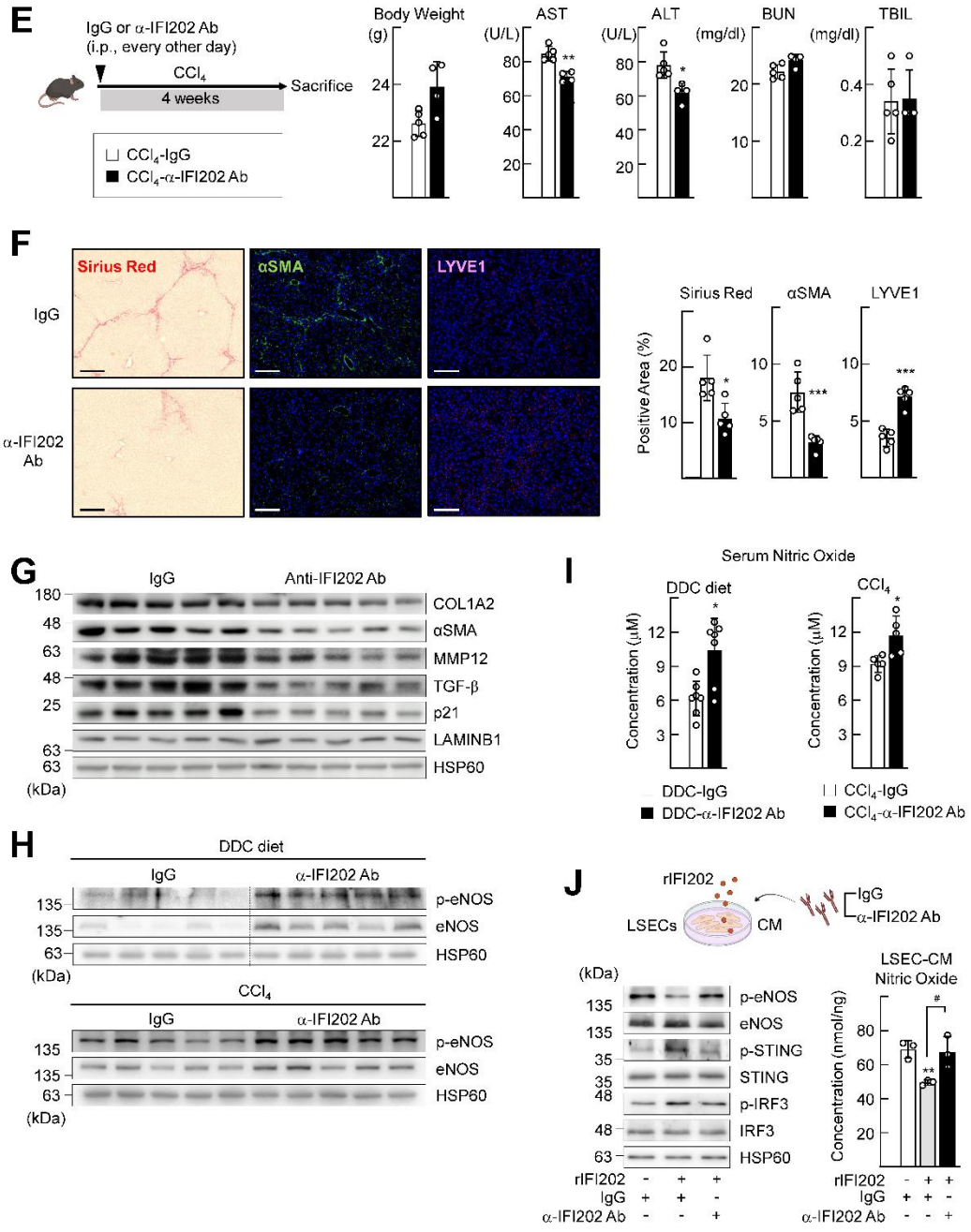
Abbreviations: pERK, phosphorylated extracellular signal–regulated kinase.

Figure 8. Lim et al



1

Figure 8. Lim et al (cont'd)



1

Figure 8. Neutralizing IFI202 antibody alleviates DDC- and CCl_4-induced liver fibrosis.

(A) Primary HSCs were seeded at 1×10^6 cells/well and cultured for 7 days, then treated with LSEC–CM preincubated for 1 h with either an anti-IFI202 Ab or an IgG. Immunofluorescence staining for αSMA (left; scale bar, 20 μm) and mRNA expression by qRT-PCR (right) were analyzed. Data are shown as mean ± SD (*n = 3* per group). Statistical significance was determined using an unpaired *t*-test, assuming a normal (Gaussian) distribution. $^{***}P < 0.001$ *vs* IgG–HSC–CM; $^{\#\#}P < 0.01$ *vs* IgG–LSEC–CM. **(B-D)** Mice were fed a 0.1% DDC diet to induce liver fibrosis and were treated with either anti-IFI202 Ab or IgG every other day. **(B)** Schematic overview of the experimental design (left). Body weight and serum AST, ALT, BUN, and total bilirubin levels were measured at the end of the experiment. Data are presented as mean ± SD (*n = 8* per group). Statistical significance was determined using the two-tailed Mann–Whitney *U* test. $^{***}P < 0.001$, $^{**}P < 0.01$ *vs* DDC–IgG (right). **(C)** Sirius Red staining, immunofluorescence for αSMA and LYVE1 were performed on liver sections to assess collagen deposition and endothelial phenotype (left; scale bar, 1 mm), with quantification shown on the right. Data are presented as mean ± SD (*n = 8* per group). Statistical significance was determined using the two-tailed Mann–Whitney *U* test. $^{***}P < 0.001$, $^{**}P < 0.01$ *vs* DDC–IgG (right). **(D)** Western blot of liver fibrosis-related proteins (COL1A2, αSMA, MMP9, MMP12, TGF-β, p21, LAMIN B1) in liver tissues (left). Expression of vascular function-related genes (*Cd209b, Plvap, Stab2, Lyve1, Nos3*) and capillarization-related genes (*Pecam1, Edn1*) were assessed by qRT-PCR (right). Data are presented as mean ± SD (*n = 8* per group). Statistical significance was determined using the two-tailed Mann–Whitney *U* test. $^{***}P < 0.001$, $^{**}P < 0.01$, $^{*}P < 0.05$ *vs* DDC–IgG. **(E-G)** Mice were treated with CCl_4 twice weekly for 4 weeks to induce liver fibrosis and were treated with either anti-IFI202 Ab or IgG every other day. **(E)** Schematic overview of the experimental design (left). Body weight and serum AST, ALT, BUN, and total bilirubin levels were measured at the end of the experiment. Data are presented as mean ± SD (*n = 4-5* per group). Statistical significance was determined using the two-tailed Mann–Whitney *U* test. $^{*}P < 0.05$, $^{**}P < 0.01$ *vs* CCl_4-IgG (right). **(F)** Sirius Red staining, immunofluorescence for αSMA and LYVE1 were performed on liver sections (left; scale bar, 0.15 mm), with quantification shown on the right. Data are presented as mean ± SD (*n = 5* per group). Statistical significance was determined using the two-tailed Mann–Whitney *U* test. $^{*}P < 0.05$, $^{***}P < 0.001$ *vs* CCl_4-IgG (right). **(G)** Western blot of liver fibrosis-related proteins in liver tissues. **(H)** Expression levels of p-eNOS and eNOS in liver tissues were measured by western blotting. HSP60 was shown as loading control. **(I)** Total amount of nitric oxide in plasma was measured. Data are presented as mean ± SD (*n = 7* and *n = 5* for DDC and CCl_4, respectively). Statistical significance was determined using the two-tailed Mann–Whitney *U* test. $^{*}P < 0.05$ *vs* IgG. **(J)** LSECs were treated with rIFI202 (2 μg/mL) and incubated for 16 h with either an anti-IFI202 Ab (10 μg/mL) or an IgG. CM was collected, and total nitric oxide levels were measured (left) and expressions of p-eNOS, eNOS, p-STING, STING, p-IRF3, IRF3 were analyzed by western blot (right). Data are presented as mean ± SD (*n = 3*). Statistical significance was

determined by unpaired *t*-test, assuming a normal (Gaussian) distribution. $^{**}P < 0.01$ *vs* IgG; $^{\#}P < 0.05$ *vs* IgG-rIFI202.

Abbreviations: CM, conditioned medium; IFI202, interferon-inducible protein 202; LYVE1, lymphatic vessel endothelial hyaluronan receptor 1; MMP12, matrix metalloproteinase 12; MMP9, matrix metalloproteinase 9.

Supplementary information

Hepatic angiokine IFI16/IFI202 couples endothelial senescence and stellate cell activation to drive liver fibrosis

Ga Young Lim[1,*], Seung-Su Kim[1,*], Ji-Eun Kim[1], Hae-Min Kwon[1], Na-Lee Ka[2], Hyun Young Kim[3,4], Hyeon-Ji Kim[1], Sang-Heon Lee[1], Cheolhee Jeong[1], Yun-Hee Lee[1,5], Won Kim[6], Jihye You[7], You Mie Lee[7], Soo Young Park[8], and Mi-Ock Lee[1,5,9,**]

[1]College of Pharmacy and Natural Products Research Institute, Seoul National University, Seoul 08826, Republic of Korea.

[2]College of Pharmacy, Duksung Women's University, Seoul 01369, Republic of Korea.

[3]College of Pharmacy, Dankook University, Cheonan 31116, Republic of Korea.

[4]Center for Human Risk Assessment, Dankook University, Cheonan, Chungnam, Republic of Korea

[5]Research Institute of Pharmaceutical Sciences, Seoul National University, Seoul 08826, Republic of Korea.

[6]Department of Internal Medicine, Seoul National University College of Medicine, SMG-SNU Boramae Medical Center, Seoul 07061, Republic of Korea.

[7]Research Institute of Pharmaceutical Sciences, College of Pharmacy, Kyungpook National University, Daegu 41566, Republic of Korea.

[8]Department of Internal Medicine, School of Medicine, Kyungpook National University, Daegu 41944, Republic of Korea.

[9]Bio-MAX institute, Seoul National University, Seoul 08826, Republic of Korea.

*Equal contribution

**Corresponding author. Tel: +82 2 880 9331; E-mail: molee@snu.ac.kr

Address correspondence to: Mi-Ock Lee Ph. D., College of Pharmacy, Seoul National University, 1 Gwanak-ro, Gwanak-gu, Seoul 08826, Republic of Korea. E-mail: molee@snu.ac.kr

Supplementary Table 1. Reagents and resources used in this study

REAGENT or RESOURCE	SOURCE	IDENTIFIER
Antibodies		
anti-IFI202	Santa Cruz Biotechnology, Dallas, TX, USA	sc-166253
anti-IFI203	Prosci, Fort Collins, CO, USA	43-316
anti-IFI204	Novus Biologicals, Centennial, CO, USA	NBP2-27153
anti-p-STING	Cell Signaling Technology, Danvers, MA, USA	85735S
anti-STING	Cell Signaling Technology	13647S
anti-IFNβ	Invitinrogen, Thermo Fisher Scientific, Waltham, MA, USA	pa5-20390
anti-HSP60	Abcam	ab45134
anti-CD146	Abcam, Cambridge, UK	ab75769
anti-COL1A2	Santa Cruz Biotechnology	sc-8787
anti-PAI-1	BD Biosciences, San Jose, CA, USA	612024
anti-GSDMD	Invitrogen	PA50116815
anti-His	Santa Cruz Biotechnology	sc-8036
anti-α-SMA	Cell Signaling Technology	19245S
anti-MMP9	Santa Cruz Biotechnology	sc-10737
anti-MMP12	Proteintech, Rosemont, IL, USA	22989-1-AP
anti-P21	Santa Cruz Biotechnology	sc-6246
anti-TGFβ	Santa Cruz Biotechnology	sc-374658
anti-p-ERK	Santa Cruz Biotechnology	sc-7383
anti-ERK	Santa Cruz Biotechnology	sc-94
anti-p-p65	Cell Signaling Technology	3033S
anti-p65	Cell Signaling Technology	19781S
anti-p-SMAD3	Cell Signaling Technology	9520S
anti-SMAD2/3	Cell Signaling Technology	3102S
anti-LAMIN B1	Abcam	ab16048
anti-cKIT	R&D Systems, Minneapolis, MN, USA	AF1356
anti-LYVE1	Abcam	ab281587
anti-p-eNOS	Cell Signaling Technology	9570
anti-eNOS	Cell Signaling Technology	32027
Virus strains		
pAAV-MCS	Cell Biolabs, San Diego, CA, USA	VPK-410

Chemicals		
Corn oil	Sigma-Aldrich	8001-30-7
CCl_4	Sigma-Aldrich	56-23-5
DDC	Sigma-Aldrich	137030
CD146 Microbeads	Miltenyi Biotec, Bergisch Gladbach, Germany	130-092-007
IFN-β	PBL Assay Science, Piscataway, NJ, USA	12410-1
Hydrogen peroxide	Sigma-Aldrich	H1009
mIL-6	PeproTech, Cranbury, NJ, USA	216-16
mTGF-β	R&D Systems	7666-MB-005
Chenodeoxycholic acid	Sigma-Aldrich	C9377
Necrosulfonamide	Sigma-Aldrich	480073
IgG isotype control	GenScript, Piscataway, NJ, USA	A01730
Lipofectamine 2000	Invitrogen	11668019
C-176	MedChemExpress	HY-112906
C29	InvivoGen.	inh-c29
OxPAPC	InvivoGen.	tlrl-oxp1
Lipofectamine 3000	Invitrogen	L3000001
Dexamethasone	Sigma-Aldrich, St. Louis, MO, USA	D4902
Easy-Blue	iNtRON Biotechnology, Seongnam, South Korea	17061
PMSF	Sigma-Aldrich	P7626
SYBR Green Master mix	Applied Biosystems, Thermo Fisher Scientific, Waltham, MA, USA	A25742
A-coated magnetic beads	GenScript, Piscataway, NJ, USA	
Insulin–transferrin–selenium	Thermo Fisher Scientific	41400045
Critical commercial assays		
Human IFI16 ELISA kit	LSBio	LS-F27011
Mouse Interferon-activable protein 202 (IFI202) ELISA Kit	Abbexa, Cambridge, UK	abx528062
Senescence Cells histochemical Staining kit	Sigma-Aldrich	CS0030
LDH cytotoxicity assay kit	Sigma-Aldrich	MAK529
Mouse IL-6 ELISA Kit	R&D Systems	M6000B
Mouse TNF-alpha ELISA Kit	R&D Systems	MTA00B
Mouse IL-1 beta/IL-1F2 ELISA Kit	R&D Systems	MLB00C
Corning® spheroid microplates	Sigma-Aldrich	4515

Isostrip Mouse Monoclonal Isotyping Kit	Roche, Basel, Switzerland	
SBA Clonotyping System-HRP kit	SouthernBiotech, Birmingham, AL, USA	
Nitric Oxide Assay Kit (Colorimetric)	Abcam	ab65328
Software and algorithms		
R	R Core Team, Vienna, Austria	4.2.2.
Alphafold2	DeepMind, London, UK; EMBL-EBI, Hinxton, Cambridgeshire, UK	
Prism	GraphPad Prism, GraphPad Software, San Diego, CA, USA	Version 9
Phenochart™	PerkinElmer, Waltham, MA, USA	Version 2
LAS-X	Leica Microsystems, Wetzlar, Germany	Version 1
Image J	National Institutes of Health	https://imagej.nih.gov/ij/
GraphPad Prism software	GraphPad Software, San Diego, CA, USA	
Others		
CDAA-HFD	Research Diets, Inc., New Brunswick, NJ, USA	A06071302
FUJI DRI-CHEM 3500s	Fujifilm, Tokyo, Japan	

1

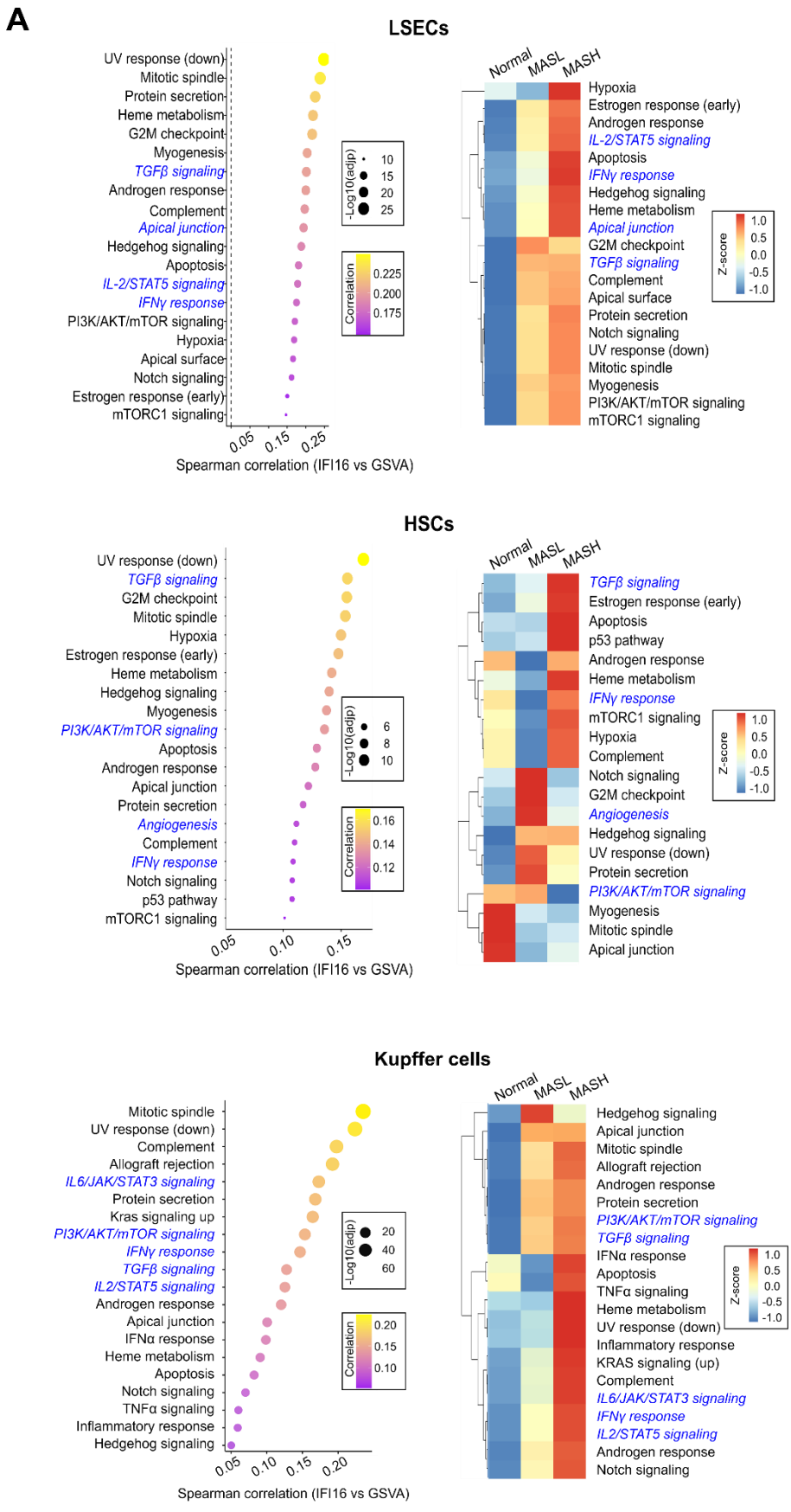
Supplementary Table 2. Oligonucleotide sequences used in the present investigation.

Purpose	Gene	Accession number		Nucleotide sequence
shRNA IFI202	*Ifi202*	NM_008327.2	Sense Antisense	5'- GAGAAAAGGAAATGGGAAACC-3' 5'- TCAATGCCACCACTTGTTTG-3'
siRNA	*GFP*		Sense Antisense	5'- GUUCAGCCUGUCCGGCGAG-3' 5'- CUCGCCGGACAGGCUGAAC-3
	TLR2-1	NM_011905.3	Sense Antisense	5- AACGAAAAGCAGAGAAGUG-3 5- CACUUCUCUGCUUUUCGUU-3´
	TLR2-2	NM_011905.3	Sense Antisense	5- AAUGAUUCUGGCUCAAAAC-3´ 5- GUUUUGAGCCAGAAUCAUU-3´
qRT-PCR	*Ifi202*	NM_008327.2	Sense Antisense	5'- GGCAATGTCCAACCGTAACT-3' 5'- TAGGTCCAGGAGAGGCTTGA-3'
	Lyve1	NM_053247.4	Sense Antisense	5'- CAGCACACTAGCCTGGTGTTA-3' 5'- CGCCCATGATTCTGCATGTAGA-3'
	Pecam1	NM_001032378.3	Sense Antisense	5'- ACCGGGTGCTGTTCTATAAGG-3' 5'- TCACCTCGTACTCAATCGTGG-3'
	Edn1	NM_010104.4	Sense Antisense	5'- CACCGTCCTCTTCGTTTTGC-3' 5'- GGCTCTGCACTCCATTCTCA-3'
	Lamb1	NM_008482.3	Sense Antisense	5'-GAAAGGAAGACCCGAAGAAAA-3' 5'-CCATAGGGCTAGGACACCAAA-3'
	Stab2	NM_138673.3	Sense Antisense	5'- AACTGGCAGTGATGTCGGAG-3' 5'- GGAGTGGAGAAACAGCTCCC-3'
	Cd209b	NM_026972.5	Sense Antisense	5'-TGGGCTCCTGCTGATCATT-3' 5'-TTCCCTTGGGAGATGGGGAT-3'
	Ehd3	NM_020578.3	Sense Antisense	5'-CGCCGTGCTTGAAAGTATCAG-3' 5'-ATAATTCGGTCCACCCGCTC-3'
	Plvap	NM_032398.2	Sense Antisense	5'-CCTGCGCTATTTCTTCCTCTT-3' 5'- CAGTTGCTGCATGACTGTTTC-3'
	Stab1	NM_138672.2	Sense Antisense	5'- TCACTGTCCCCACACTACTTT -3' 5'- TGTCGCAACGTTTAGACCGTA -3'
	Nos3	NM_008713.4	Sense Antisense	5'- TGAGTTCAGAGATTGGCATGAG-3' 5'- CTTGATGGAAGACAGGAGTTAGG-3'
	Cdkn2a	NM_001040654.1	Sense Antisense	5'-CGAACTCGAGGAGAGCCATC-3' 5'-TACGTGAACGTTGCCCATCA-3'
	Cdkn1a	NM_007669.5	Sense Antisense	5'-AAGTGTGCCGTTGTCTCTTC -3' 5'-AGTCAAAGTTCCACCGTTCTC-3'

Supplementary Table 3. Top 21 transcripts differentially expressed in fibrotic human livers relative to healthy livers across three datasets

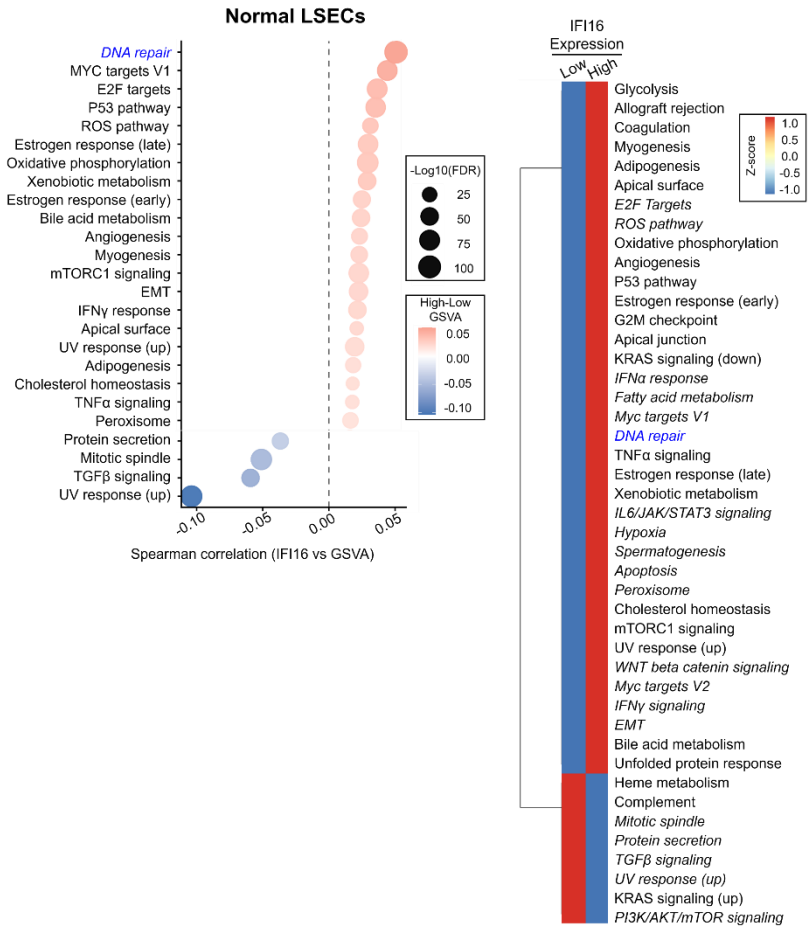
Gene symbol	Full Name	Accession number	Fold Change
			GSE206364
COL4A2	Collagen Type IV Alpha 2 Chain	NM_001846.4	2.76
TPM1	Tropomyosin 1	NM_001018005.2	1.78
GSN	Gelsolin	NM_198252.3	2.16
COL4A1	Collagen Type IV Alpha 1 Chain	NM_001845.5	2.85
PACS1	Phosphofurin Acidic Cluster Sorting Protein 1	NM_018026.4	1.30
IFI16	Interferon Gamma Inducible Protein 16	NM_005531.5	2.23
UGCG	UDP-Glucose Ceramide Glucosyltransferase	NM_003358.3	1.70
SEL1L3	SEL1L Family Member 3	NM_015187.5	2.12
HKDC1	Hexokinase Domain Containing 1	NM_025130.4	3.98
CBLB	Casitas B-Lineage Lymphoma Proto-Oncogene B	NM_170662.5	1.86
GLS	Glutaminase	NM_014905.5	2.04
RAB8B	RAB8B, Member RAS Oncogene Family	NM_016530.3	1.79
DCDC2	Doublecortin Domain Containing 2	NM_016356.5	3.75
BACE2	Beta-Secretase 2	NM_012105.5	2.37
SLCO3A1	Solute Carrier Organic Anion Transporter Family Member 3A1	NM_013272.4	1.77
BICC1	BicC Family RNA Binding Protein 1	NM_001080512.3	3.11
GPRIN3	G Protein Regulated Inducer of Neurite Outgrowth 3	NM_198281.3	3.61
DTNA	Dystrobrevin Alpha	NM_001386795.1	3.82
ARHGEF3	Rho Guanine Nucleotide Exchange Factor 3	NM_019555.3	2.61
SLC22A15	Solute Carrier Family 22 Member 15	NM_018420.3	3.83

Supplementary Figures

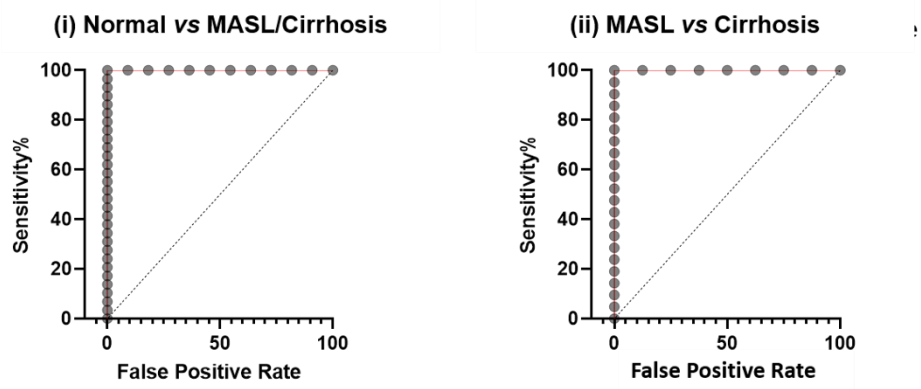


1

B



C

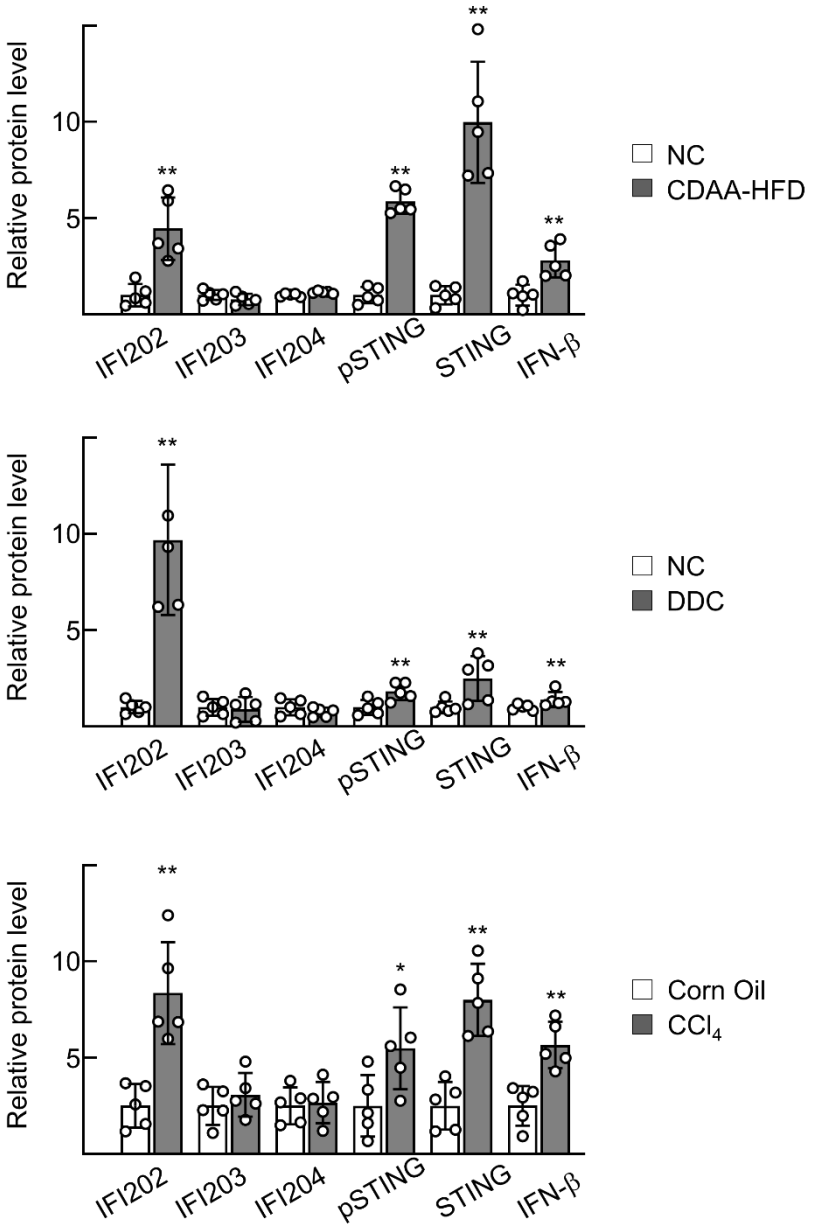


Area	1.000
Std. Error	0.000
95% confidence interval	1.000 to 1.000
P value	<0.0001

Area	1.000
Std. Error	0.000
95% confidence interval	1.000 to 1.000
P value	<0.0001

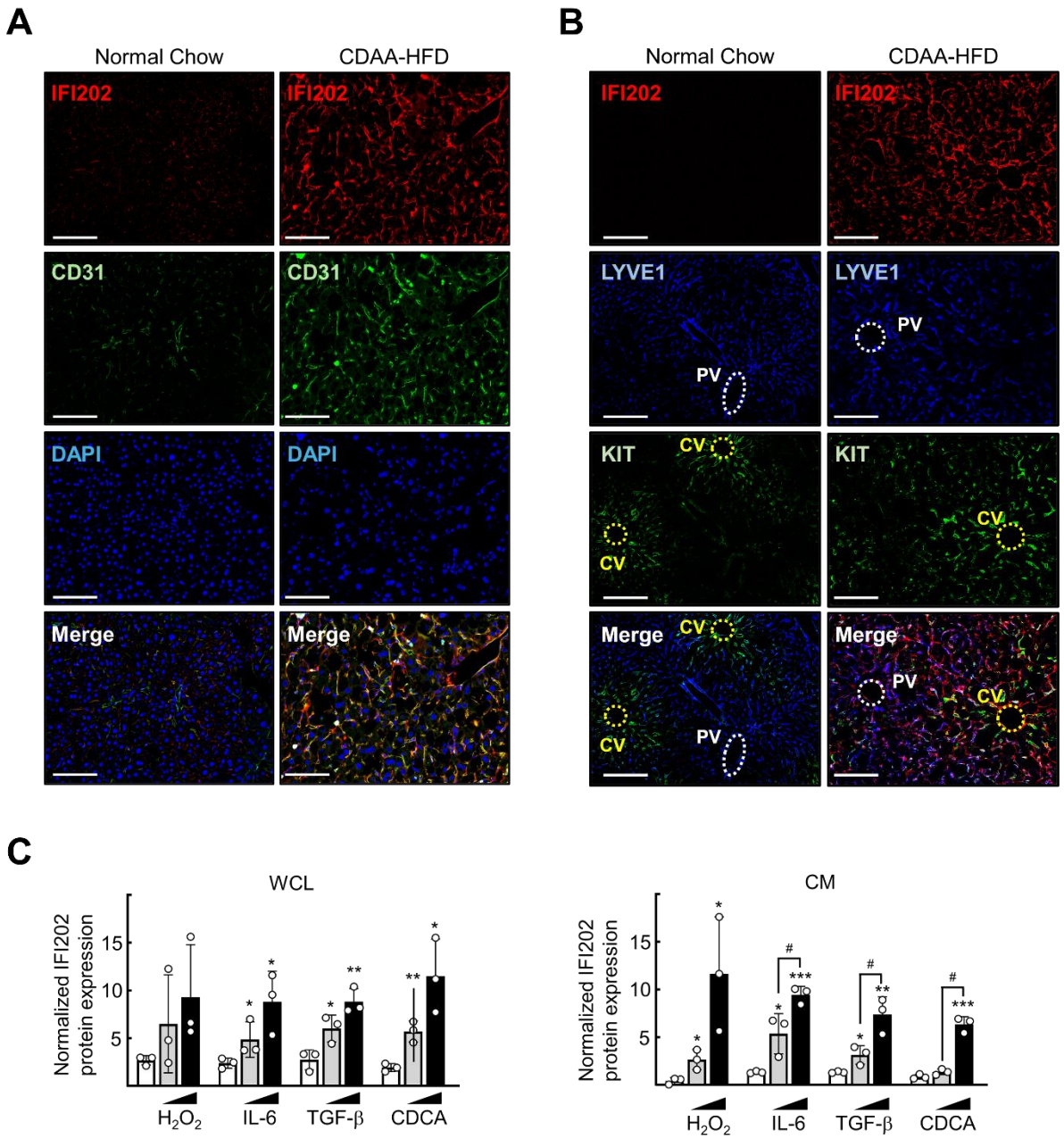
Supplementary Figure 1: IFI16-associated transcriptional programs in LSECs, HSCs and Kupffer cells across disease progression.

(A) IFI16-associated transcriptional programs in LSECs, HSCs and Kupffer cells across disease progression. Dot plots and heatmaps showing IFI16-associated gene sets identified by GSVA and correlation analysis in LSEC (top), HSC (middle) and Kupffer cells (bottom). Dot plots display the Hallmark gene sets positively correlated with IFI16 expression, ranked by Spearman correlation coefficient. Dot size represents statistical significance (−log10 adjusted p-value), and color indicates the strength of correlation. Corresponding heatmaps illustrate the average GSVA scores of these gene sets across disease conditions (Normal, MASL, and MASH), scaled by row. Rows represent gene sets, and columns represent disease conditions. **(B)** Physiological pathways associated with IFI16 expression in normal LSECs. A total of 7,395 endothelial cells were identified, of which 1,638 cells exhibited detectable IFI16 expression (IFI16 > 0). IFI16-positive endothelial cells were stratified into IFI16-low (*n = 410*) and IFI16-high (*n = 411*) groups using the lower and upper quartiles of log-normalized IFI16 expression (Q1 = 1.724, Q3 = 2.443), while cells with intermediate IFI16 expression (*n = 817*) were excluded from the comparison. Differential pathway activity between IFI16-high and IFI16-low LSECs was evaluated using the Wilcoxon rank-sum test followed by Benjamini–Hochberg multiple-testing correction. Forty-five Hallmark pathways were significantly altered at an FDR < 0.05. The heatmap displays row-scaled mean GSVA scores for representative pathways, whereas the accompanying dot plot shows the top 21 pathways ranked by statistical significance and effect size. Dot color represents the mean GSVA score difference between IFI16-high and IFI16-low LSECs (High − Low), and dot size represents the statistical significance (−log10 adjusted P value). **(C)** Receiver operating characteristic (ROC) curve analysis of circulating IFI16 levels in patients with MASLD. ROC curve analysis was performed to evaluate the diagnostic performance of serum IFI16 levels. (i) ROC curve distinguishing healthy controls from patients with liver disease (MASL and cirrhosis). (ii) ROC curve distinguishing patients with MASL from those with cirrhosis. The area under the ROC curve (AUC), 95% confidence intervals, and corresponding *P* values are indicated in each panel.



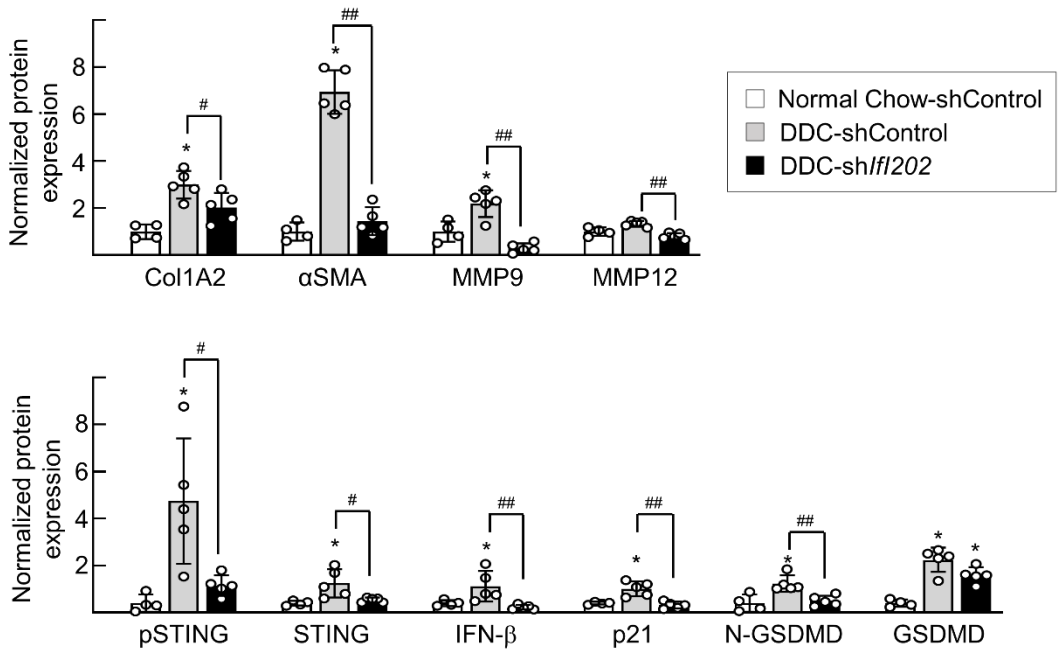
Supplementary Figure 2: Hepatic IFI202 expression is induced after fibrotic liver injury in mice (related to Figure 2).

Band intensities of western blot images shown in Figure 2A, 2B, and 2C were quantified using ImageJ software (National Institutes of Health). Data are presented as mean ± SD, $n = 5$ per group. Statistical significance was assessed using the two-tailed Mann–Whitney U test. $^{**}P < 0.01$ *vs* normal chow (NC) or corn oil, $^{*}P < 0.05$ *vs* NC or corn oil.



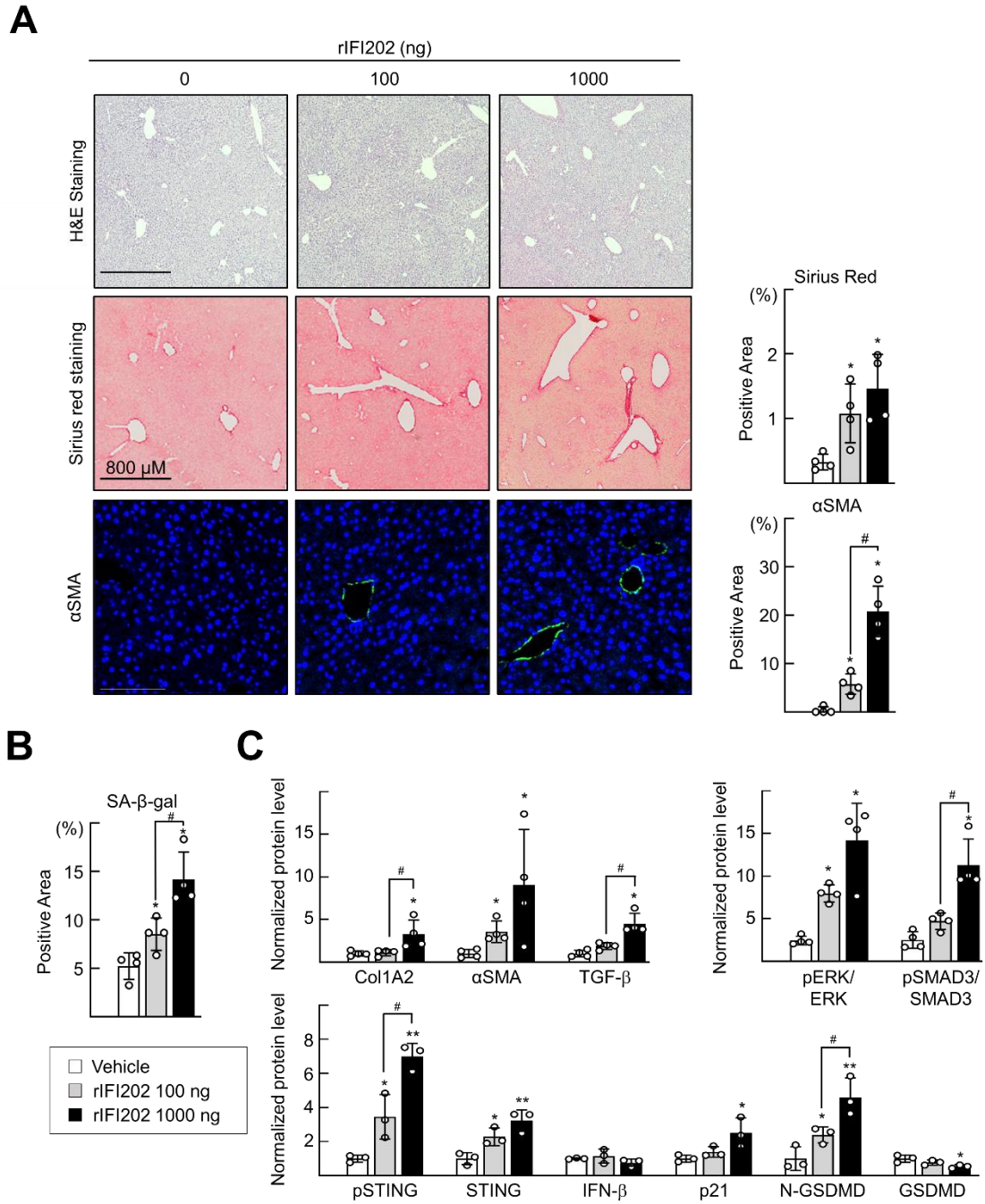
Supplementary Figure 3: Expression and secretion levels of IFI202 were elevated in primary LSECs upon stimulation with fibrogenic stimuli (related to Figure 3).

(**A, B**) Representative immunofluorescence images of liver sections from mice fed a CDAA-HFD. IFI202 (red), CD31 (green), and merged images (**A**). IFI202 (red), LYVE1 (blue), KIT (green), and merged images (**B**). Scale bar, 100 μm. (**C**) Band intensities of western blot images shown in Figure 3E was quantified using ImageJ software. Data are presented as mean ± SD (*n = 3*). Statistical significance was determined by unpaired *t*-test. $^{***}P < 0.001$ *vs* vehicle; $^{**}P < 0.01$ *vs* vehicle; $^{*}P < 0.05$ *vs* vehicle; $^{\#}P < 0.05$ *vs* the corresponding intermediate-dose group.



Supplementary Figure 4: Fibrotic liver injury induces IFI202 expression in the mouse liver (related to Figure 5)

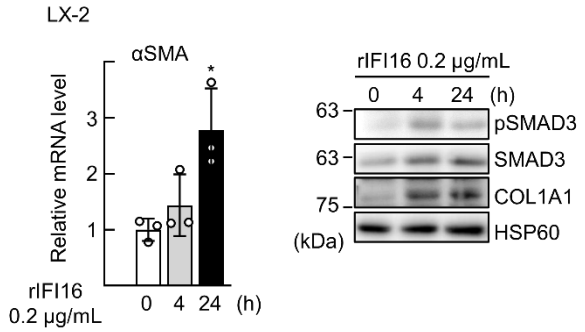
Band intensities of western blot images shown in Figures 5B and 5C were quantified using ImageJ software. Data are presented as mean ± SD (*n = 4, 5, and 5* per group). Statistical significance was performed using the two-tailed Mann–Whitney *U* test. $^{*}P < 0.05$ *vs* NC–shControl; $^{\#\#}P < 0.01$ *vs* DDC–shControl; $^{\#}P < 0.05$ *vs* DDC–shControl.



1 **Supplementary Figure 5: Injection of IFI202 induces fibrotic changes in the liver (related to**
2 **Figure 6).**

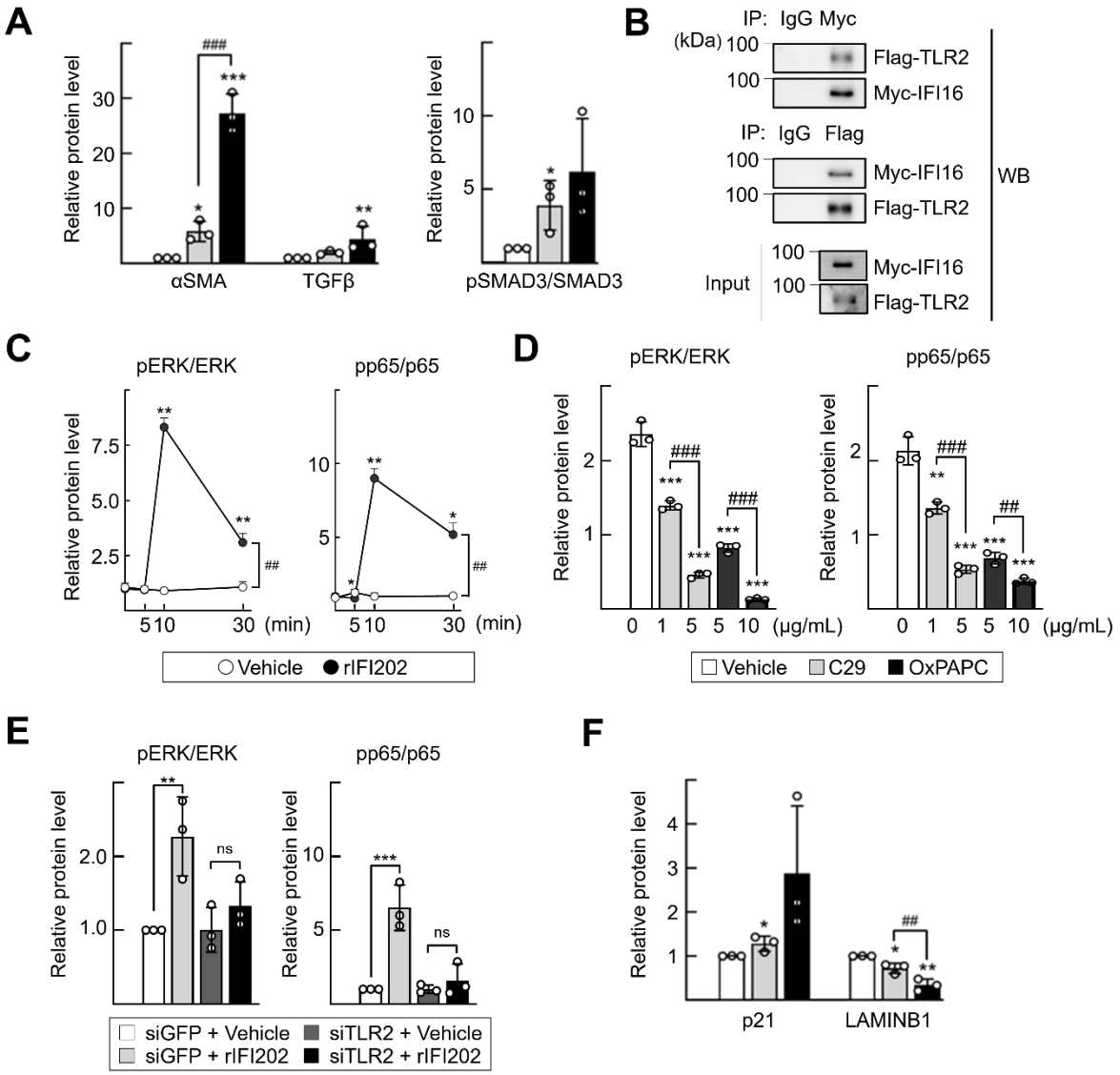
3 (**A**) Representative images of liver sections stained with Sirius Red (top), immunofluorescence for
4 αSMA (middle), H&E (bottom), scale bar, 800 µm (left). Staining intensity was quantified from four
5 liver samples per group using ImageJ software (right). Data are presented as mean ± SD (*n = 4* per
6 group). Statistical analyses were performed using the two-tailed Mann–Whitney *U* test. $^{*}P < 0.05$ *vs*
7 Vehicle; $^{\#}P < 0.01$ *vs* rIFI202 100 ng. **(B)** Quantification of senescence associated-β-galactosidase (SA-
8 β-gal)–positive cells corresponding to Figure 6D. Data are presented as mean ± SD (*n = 4* per group).
9 Statistical analyses were performed using the two-tailed Mann–Whitney *U* test. $^{*}P < 0.05$ *vs* Vehicle;

$^{\#}P < 0.05$ *vs* rIFI202 100 ng. **(C)** Band intensities of western blot images shown in Figures 6C and 6D were quantified using ImageJ software. Data are presented as mean ± SD ($n = 4$ per group). Statistical analysis was performed using the two-tailed Mann–Whitney *U* test. $^{**}P < 0.01$ *vs* Vehicle, $^{*}P < 0.05$ *vs* Vehicle; $^{\#}P < 0.05$ *vs* rIFI202 100 ng.



Supplementary Figure 6: IFI16 upregulated αSMA, COL1A1 and TLR2 downstream signaling in LX-2 human HSCs.

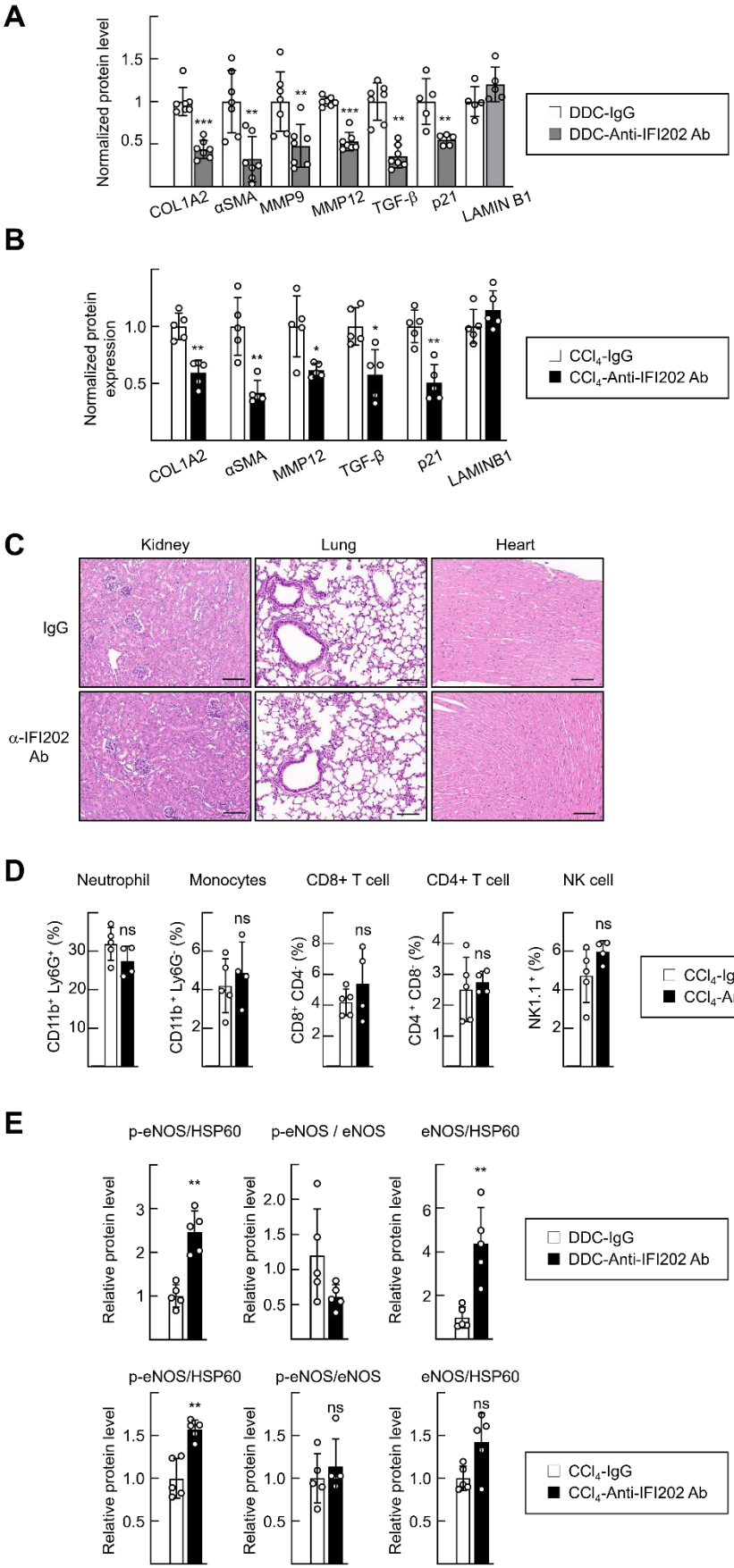
LX-2 cells (2×10^5 cells/well) were treated with recombinant human IFI16 (rIFI16; 0.2 μg/mL; OriGene) and harvested at 0, 4, and 24 h. The mRNA expression level of αSMA was analyzed by qRT-PCR (left). Data are presented as mean ± SD (*n = 3*). Statistical significance was determined using an unpaired *t*-test. $^{*}P < 0.05$ *vs* 0 h. Protein expression levels of pSMAD3, total SMAD3, and COL1A1 were assessed by western blotting (right). HSP60 was used as a loading control.



Supplementary Figure 7: rIFI202 induces TLR2-mediated activation of HSCs and senescence of LSECs (related to Figure 7).

(**A**) Band intensities of western blot images shown in Figure 7A were quantified using ImageJ software. Data are presented as mean ± SD (*n = 3*). Statistical significance was determined by unpaired *t*-test. $^{***}P < 0.001$ *vs* 0 h, $^{**}P < 0.01$ *vs* 0 h, $^{*}P < 0.05$ *vs* 0 h; $^{###}P < 0.001$ *vs* 0 h. (**B**) Immunoprecipitation was performed using whole cell lysates from LX-2 cells overexpressing Myc-IFI16 and Flag-TLR2 using anti-Flag or anti-Myc antibodies, and the precipitated proteins were analyzed by western blot. **(C)** Band intensities of western blot images shown in Figure 7B were quantified using ImageJ software. Data are presented as mean ± SD (*n = 3* per group). Statistical significance was determined by two-way ANOVA with Bonferroni post hoc tests. $^{**}P < 0.01$, $^{*}P < 0.05$ *vs* Vehicle of each time point; $^{##}P < 0.01$ *vs* Vehicle. (**D**) Band intensities of western blot images shown in Figure 7C (left) were quantified using ImageJ software. Data are presented as mean ± SD (*n = 3* per group). Statistical significance was determined by unpaired *t*-test. $^{***}P < 0.001$ *vs* Vehicle, $^{**}P < 0.01$ *vs* Vehicle; $^{###}P < 0.001$ *vs* C29 1

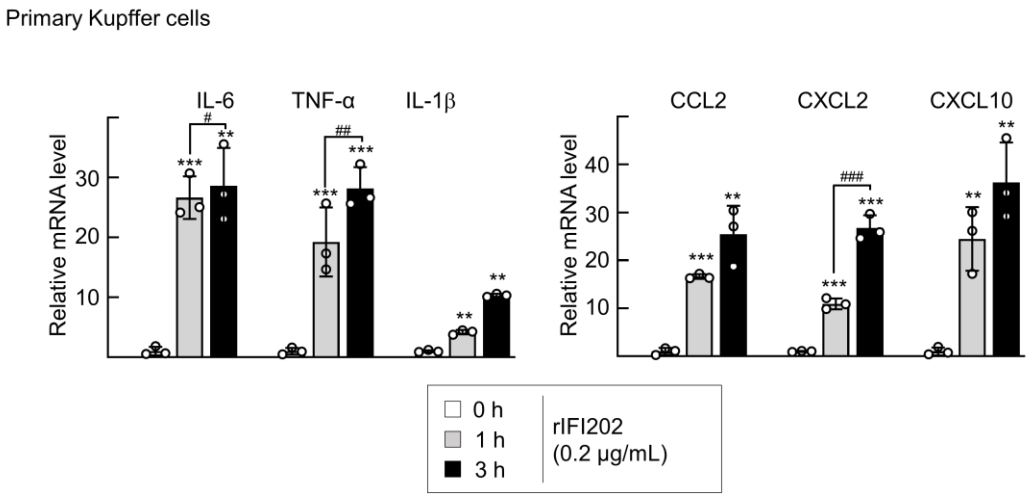
μg/mL or OxPAPC 5 μg/mL, $^{\#\#}P < 0.01$ *vs* C29 1 μg/mL or OxPAPC 5 μg/mL. **(E)** Band intensities of western blot images shown in Figure 7C (right) were quantified using ImageJ software. The level of TLR2 proteins were suppressed by 79.1 ± 1.9% (mean ± SD, $n = 3$) in this siRNA approach. Data are presented as mean ± SD ($n = 3$). Statistical significance was determined by unpaired *t*-test. $^{**}P < 0.01$ and $^{***}P < 0.001$. ns, not significant. **(F)** Band intensities of western blot images shown in Figure 7D were quantified using ImageJ software. Data are presented as mean ± SD ($n = 3$). Statistical significance was determined by unpaired *t*-test. $^{**}P < 0.01$ *vs* 0 μg/mL, $^{*}P < 0.05$ *vs* 0 μg/mL; $^{\#\#\#}P < 0.001$ *vs* 0.2 μg/mL, $^{\#\#}P < 0.01$ *vs* 0.2 μg/mL.


A
Normalized protein level
1.5
1
0.5
COL1A2
αSMA
MMP9
MMP12
TGF-β
p21
LAMIN B1
DDC-IgG
DDC-Anti-IFI202 Ab
B
Normalized protein expression
1.0
0.5
COL1A2
αSMA
MMP12
TGF-β
p21
LAMINB1
CCl4-IgG
CCl4-Anti-IFI202 Ab
C
Kidney
Lung
Heart
IgG
α-IFI202 Ab
D
Neutrophil
Monocytes
CD8+ T cell
CD4+ T cell
NK cell
CD11b+ Ly6G+ (%)
CD11b+ Ly6G- (%)
CD8+ CD4- (%)
CD4+ CD8- (%)
NK1.1+ (%)
ns
CCl4-IgG
CCl4-Anti-IFI202 Ab
E
p-eNOS/HSP60
p-eNOS / eNOS
eNOS/HSP60
Relative protein level
**
DDC-IgG
DDC-Anti-IFI202 Ab
p-eNOS/HSP60
p-eNOS/eNOS
eNOS/HSP60
ns
CCl4-IgG
CCl4-Anti-IFI202 Ab

1

Supplementary Figure 8: IFI202 neutralization attenuates fibrosis-related gene expression without apparent systemic or immunological effects.

(**A**) Band intensities of western blot images shown in Figure 8D were quantified using ImageJ software. Data are presented as mean ± SD (*n = 7* per group). Statistical significance was performed using two-tailed Mann–Whitney *U* test. $^{***}P < 0.001$ *vs* DDC–IgG, $^{**}P < 0.01$ *vs* DDC–IgG. **(B)** Band intensities of western blot images shown in Figure 8G were quantified using ImageJ software. Data are presented as mean ± SD (*n = 5* per group). Statistical analysis was performed using the Mann–Whitney *U* test. $^{*}P < 0.05$, $^{**}P < 0.01$ *vs* CCl_4–IgG. **(C)** Representative H&E-stained sections of the heart, lung, and kidney from CCl_4-treated mice treated with IgG or anti-IFI202 neutralizing antibody. Scale bars, 100 μm. **(D)** Flow-cytometric analysis of peripheral blood leukocytes from mice treated with CCl_4 together with control IgG or a neutralizing anti-IFI202 antibody for 4 weeks. The frequencies of neutrophils ($CD11b^+Ly6G^+$), monocytes ($CD11b^+Ly6G^-$), $CD8^+$ T cells ($CD8^+CD4^-$), $CD4^+$ T cells ($CD4^+CD8^-$), and NK cells ($NK1.1^+$) are shown as percentages of $CD45^+$ cells. Data are presented as individual values with mean ± SEM. ns, not significant. **(E)** Band intensities of western blot images shown in Figure 8H were quantified using ImageJ software. Data are presented as mean ± SD (*n = 5* per group). Statistical analysis was performed using the Mann–Whitney *U* test. $^{*}P < 0.05$, $^{**}P < 0.01$ *vs* DDC-IgG or CCl_4–IgG.



Supplementary Figure 9: IFI202 induces proinflammatory cytokines and chemokines in KCs. Primary KCs (1×10^6 cells/well) were treated with recombinant mouse IFI202 (rIFI202; 0.2 μg/mL) and harvested at 0, 1, and 3 h. The mRNA expression levels of proinflammatory cytokines and chemokines were measured by qRT-PCR. Data are presented as mean ± SD (*n* = *3*). Statistical significance was assessed using an unpaired *t*-test. $^{***}P < 0.001$ *vs* 0 h, $^{**}P < 0.01$ *vs* 0 h; $^{###}P < 0.001$ *vs* 1 h, $^{##}P < 0.01$ *vs* 1 h, $^{#}P < 0.05$ *vs* 1 h.